nature astronomy

Supplementary information

https://doi.org/10.1038/s41550-025-02746-w

A possible challenge for cold and warm dark matter

In the format provided by the authors and unedited

Supplementary Information

Comparison with dark matter models

We have tested 23 models for the mass density profiles of detection $\mathcal{V}$. Here, we discuss in more detail the implications of its inferred structure for the nature of dark matter, assuming that it is a dark matter-dominated object. Given the area of sky probed by the data, Powell et al. [1] have estimated the probability of detecting at least one subhalo with a mass between 10^6 $M_\odot$ and 10^7 $M_\odot$ to be 0.65 and 0.14, for CDM and for WDM with $m_{\rm wdm} = 4.6$ keV, respectively. Hence, detecting such an object is not *a priori* unlikely. However, we find that in CDM or WDM models, its predicted structure is incompatible with that inferred for our VLBI detection (see Extended Data Figure 2).

The $\rm NFW_{field}$ halo has a fitted concentration of $\log c_{\rm vir} = 2.91 \pm 0.09$. A CDM NFW halo with a mass and redshift consistent with our analysis ($M_{\rm vir} \sim 2.9 \times 10^6 M_\odot$ and $z \sim 1.4$) is expected to have a virial concentration of $\log c_{\rm vir} = 1.10 \pm 0.15$ [2] or $\log c_{\rm vir} = 1.04 \pm 0.09$ [3], depending on the assumed concentration-mass relation. Hence, the mean log inferred value is 10 or 14σ larger than the median of the lognormal distributions predicted by N-body simulations; here σ is the sum in quadrature of the uncertainty on the inferred value and the scatter in the lognormal relations. Similarly, the NFW subhalo model has a $\log c_{\rm v} = 7.25 \pm 0.17$, which is 20σ larger than the median value of $\log c_{\rm v} = 3.90 \pm 0.02$ [4] predicted for a subhalo with a peak circular velocity of $V_{\rm max} = 7.98$ km s^{-1} and peak radius $\rm r_{max} = 24$ pc at z =0.881.

To quantify the statistical level at which the CDM model is incompatible with the data, we consider two extra models, $\rm NFW_{CDM,field}$ and $\rm NFW_{CDM}$. The former has a free redshift and $c_{\rm vir}$ drawn from a lognormal distribution with median and scatter taken from numerical simulations [specifically from 2]. The second model assumes the perturber to be at the same redshift as the lens, and its $r_{\rm max}$ is drawn from a lognormal distribution with median and scatter taken from [4]. The $\rm NFW_{CDM,field}$ model prefers a halo at z = 0.883 ± 0.028 (this is consistent with the lens redshift within uncertainties) with $M_{\rm vir} = (4.04 \pm 0.27) \times 10^6 M_\odot$ and $\log c_{\rm vir} = 2.18 \pm 0.04$, but with $\Delta \ln \mathcal{E} = -75$. The subhalo model $\rm NFW_{CDM}$ gives a best fit for a subhalo with $\rm M_{max} = (8.13 \pm 0.27) \times 10^5 M_\odot$ within $r_{\rm max} = 85.0 \pm 5.7$ pc, but with $\Delta \ln \mathcal{E} = -147$. In both cases, the inferred concentrations are very far out in the high-concentration tail of the predicted distributions, leading to the models being very strongly disfavoured, at a level between 12 and 17σ. We note that the relatively low redshift inferred for $\rm NFW_{CDM,field}$ is due to a combination of the redshift dependence of the mass concentration relation and the fact that most of the prior volume is at relatively low concentration values; that is, perturbers at lower redshift can provide a similar lensing effect to higher redshift ones for a smaller and hence more probable concentration (Tajalli et al. in prep.).

Once a point mass is added to the NFW model, we infer smaller concentrations for the extended component, $\log c_{\rm V} = 5.36 \pm 0.20$ at $z \equiv z_{\rm lens}$ and $\log c_{\rm vir} = 1.69 \pm 0.08$ at $z = 0.925 \pm 0.059$. These values are nominally 6 and 3σ larger than the predicted values for dark-matter-only objects of the same mass and redshift, but a direct comparison to such predictions is not appropriate. This is because a central black

hole would substantially increase the concentration of a dark matter halo, reducing or eliminating the conflict with our observational data, and more importantly, because our inferred black hole masses are much larger than is plausible in CDM haloes of such low mass, which, in addition, are not even expected to form stars. Ultimately, however, all variations of the NFW models are highly disfavoured by the data when compared to the best-fitting UD+PM model. Hence, we conclude that if our detection is confirmed to be dark-matter dominated, it will rule out CDM at a statistical level between 8 and 17σ, and WDM with even higher significance, increasing with decreasing particle mass.

Existing gravothermal fluid models [e.g. 5], semi-analytical models [e.g. 6, 7] and N-body simulations [e.g. 8] indicate that SIDM haloes can have density profiles with super-isothermal slopes in their inner regions once they are deep in the core collapse phase of their evolution. To investigate whether the properties of detection $\mathcal{V}$ are consistent with SIDM expectations, we focus on the gravothermal fluid model by [5]. Specifically, we fit the mass density profile at the latest available time for their $n = 3.7$ model (their Figure E1) and derive from it the corresponding projected "circular velocity" profile, defined as $V_{\rm c}(x)/V_{\rm max} = 0.61\sqrt{M_{\rm cyl}(x)/(\rho_{\rm s} r_{\rm s}^3 x)}$, with $x = R/r_{\rm s}$. Here ρ_s, $r_{\rm s}$ and $V_{\rm max}$ should be understood to be the parameters of the NFW halo in the absence of dark-matter interactions. Since fluid models, such as the one considered here, follow the evolution of idealised haloes decoupled from their cosmological context, these NFW equivalent parameters are independent of time. This is in contrast to "real" CDM haloes that grow substantially in time through accretion and merging. However, we know of no cosmological SIDM simulations with spatial resolution adequate for comparison with the VLBI data. Hence, we cannot determine how the structure of an SIDM halo with mass as small as detection $\mathcal{V}$ has been affected by the fact that it has assembled progressively with time rather than being present, effectively in isolation, since some early epoch. We therefore take $V_{\rm max}$ and $r_{\rm max}$ (equivalently $\rho_{\rm s}$ and $r_{\rm s}$) to be the values for a z = 0.881 CDM analogue, which we assume to have evolved in isolation for the Hubble time at redshift z. This is likely to overestimate the structure modification due to self-interactions, so the cross-sections needed to match the observation can be taken as lower limits on those needed in a more realistic halo assembly model.

Our best-fitting model, UD+PM, is most robustly constrained at a radius of 90 pc, with $V_{\rm c}(90\ {\rm pc}) = 7.47 \pm 0.12$ km s^{-1}. Extended Data Figure 3 shows circular velocity profiles for SIDM haloes with differing masses, together with those of their CDM analogues. The mass-concentration relation of the latter is assumed to be given by the median estimated by [2] at z = 0.881. We find that an SIDM profile will have $V_{\rm c}$ at 90 pc matching the observed value if its CDM analogue has $V_{\rm max} = 4.80$ km s^{-1} and $r_{\rm max} = 0.60$ kpc. Assuming this halo has been evolving for the age of the Universe at $z = 0.881$ and adopting the normalising time-scale by [5] gives a lower limit on the effective cross-section of $\sigma_{\rm c,0}/m_{\rm dm} = 796$ cm^2 g^{-1}. We caution, however, that this number is proportional to $V_{\rm max}^{-3} r_{\rm max}^2$ and so is very sensitive to the assumed $V_{\rm max}$–$r_{\rm max}$ relation and its scatter.

Looking more closely at Extended Data Figure 3, it can be seen that the theoretical SIDM profile is not a good match to that inferred from the observations; its mean

slope over the observationally well-determined range is significantly shallower. Soon after the time shown, the SIDM model will form a black hole, which will then grow rapidly through Bondi accretion, potentially reaching masses similar to that of the central component of our UD+PM model. Unfortunately, however, there are no reliable calculations of this initial black hole growth phase, and so, no detailed predictions of the post-collapse $M_{\rm cyl}(R)$ that we can compare with the data. The discrepancy in slope between our observations and the predictions from [5] may be related to the fact that their profile is that of an idealised isolated SIDM halo that is still in the long-mean-free-path stage of its evolution. Gad-Nasr et al. [9] have simulated even later (but still pre-collapse) phases, where the inner regions are deep into the short-mean-free-path regime. Their work offers some indication that it may be possible to achieve profile shapes similar to those required observationally for appropriately chosen velocity-dependent cross-sections. Verifying this must await simulations, which can follow evolution through black hole formation and the subsequent Bondi accretion phase. Only then will it be possible to tell whether objects with the structure observed for detection $\mathcal{V}$ can form naturally in a SIDM-dominated Universe, and, if so, what parameters this requires for the scattering cross-section.

Comparison with GCs and UCDs

In the mass range relevant for our main lens, the number of globular clusters (GCs) in a galaxy is expected to be significant and, in some cases, comparable to the number of dark matter subhaloes and field haloes [10]. The lens galaxy in the gravitational lens system JVAS B1938+666 is an early-type that has a stellar mass within the Einstein radius of $4.7{\times}10^{10} M_\odot$ [11], which implies a total number of GCs around 250 [10]. Assuming that the spatial density of the GCs follows a Sérsic profile with the same index and effective radius as the host galaxy [12] and adopting the mass function by Jordán et al. [13], we estimate a density of about 100 GCs per square arcsec in an annulus of 5 milli-arcseconds around the lensed images. As a comparison, the expected number density of subhaloes within the same area and between (10^6 to $10^9 M_\odot$) is $(9.46 \pm 0.04) \times 10^5$ $\mathrm{f_{sub}^{-1}}$ arcsec^{-2} or $(1.135 \pm 0.005) \times 10^4$ per square arcsec for a dark matter fraction in substructure of 0.012 [14], where the error reflects the uncertainty on the total lens mass. Given the lens and source redshifts, field haloes are expected to be roughly an order of magnitude more numerous [15]. Only a fraction of haloes and subhaloes are expected to core-collapse and so be detectable through their lensing effect. Hence, the relative probability of detecting a dark matter halo or a GC and an ultracompact dwarf (UCD) will depend on the details of the dark-matter model, on the as-yet unknown fraction of dark matter in subhaloes, as well as on the exact sensitivity of the data to the presence of each population.

The KG models we use to describe typical GCs are all strongly disfavoured. Those highest in the ranking are KG_∞ and KG, which have a very similar $\Delta \ln \mathcal{E}$ of -52 and -53, respectively. The characteristics of these two models that are best constrained are $\mathrm{M_{cyl,90}} \simeq 10^6$ $\mathrm{M}_\odot$ and $\mathrm{r_c} \simeq 10$ pc. Although rare, Milky Way GCs exhibiting similar properties exist, the closest example being NGC 2419, a GC located in the distant Galactic halo [16]. In fact, according to the Baumgardt catalogue of Milky Way GCs, NGC 2419 has a current mass of $\sim 8 \times 10^5$ $\mathrm{M}_\odot$ (and an initial mass, decreased by

internal dynamical processes, of 1.4×10^6 $M_\odot$) and a core radius of 8.3 pc. The KG_{td} model is even more strongly disfavoured, and has a concentration that is very small for a GC of its mass (see Extended Data Figure 1, panel (a)). Massive clusters tend to have shorter internal dynamical timescales ([see e.g., 17]), which favours evolution of the cluster structure towards higher concentration (as shown by the trend in panel (a) of Extended Data Figure 1). To be this massive yet with such low concentration, a cluster would have to be born already extended [lower stellar density implies longer dynamical timescales, 18]. The closest example to this case is once again NGC 2419, which has the longest relaxation time at the half-light radius [17] among all Milky Way GCs. Our KG_{td} model is even less concentrated than this exceptional cluster.

It is worth noting that a recent exploration of resolved Milky Way GCs has confirmed that the structural parameters recovered with the unprecedentedly deep *Euclid* photometry are in good agreement with previous studies based on brighter, more massive stars. Even including stars with a mass as low as 0.16 $M_\odot$, deviations from standard King models only become mildly relevant in the outermost regions, close to the cluster tidal radius [19]. This can affect the size of the tidal radius only by up to 20%. Given all these considerations and the fact that the KG_{td} and KG models are both strongly disfavoured by the data (although at very different levels), we deem it highly unlikely that the object under study is a GC, even if its recovered properties are not completely out of the range of those observed in the Milky Way.

UCDs were discovered in the early 2000s [20–22] as a new class of object whose properties lie between those of GCs and dwarf galaxies: their effective radii span an approximate range between 10 and 100 pc, they have stellar masses between 10^6 and 10^8 $M_\odot$, and typical luminosities of $L \sim 10^7 L_\odot$ [e.g. 23–26]. They are some of the most compact stellar systems currently known, and even though they were initially discovered in galaxy clusters, they have since been observed in lower-density environments also [27]. Different mechanisms have been proposed for the formation of different subgroups of UCDs [e.g. 27–29]. According to one of these scenarios, some UCDs arise from the tidal stripping of dwarf galaxies; what is observed today is then the remnant stellar core of the parent object [e.g. 22, 30–34]. This hypothesis is supported by observations in the local Universe of UCDs with extended envelopes (eUCDs) and tidal features, as well as with a central super-massive black hole. Single-component profiles, such as a King, a Sérsic or a de Vaucouleurs profile, describe well the light distribution of regular UCDs. However, in the case of eUCDs, they assume extreme parameters, such as poorly bounded tidal radii and very large concentrations (~ 3) for a King profile, and large indices of around 8 for a Sérsic profile [35]. This behaviour is similar to that displayed by our KG and SER models. As shown in panel (b) of Extended Data Figure 1, if we assume that the total mass of the SER model is in stars, the object under study has a size and mass which lie on the edge of the distribution of these properties for eUCDs in the Virgo Cluster.

Our profile modelling for detection $\mathcal{V}$ strongly supports an additional unresolved central component, however, and such a structure is much more compatible with the properties of a subset of UCDs that contain a compact nuclear star cluster (NSC). For example, our top model in the ranking (UD+PM) has a mass and a size entirely consistent with the nucleated UCD population in the Virgo cluster (see the black

symbol in panel (b) of Extended Data Figure 1). Moreover, the inferred ratio between the masses of the two components is consistent with observations of the inner regions of at least some UCDs hosting a NSC [36]. The starkest inconsistency between the properties of our favoured model and those observed in UCDs is the sharp mass cut-off beyond 90 pc, as shown in panel (a) of Supplementary Figure 1. This is challenging on astrophysical grounds, but could be due to the limitations of the macro-model for the main lens on these small angular scales, or to some unmodelled line-of-sight process affecting the radio data. The latter seems less likely given the observed surface brightness distribution of the gravitational arc. UCDs and eUCDs have so far been observed only within galaxy clusters, which may also disfavour this interpretation. Ultimately, only a meaningful limit on the luminosity of detection $\mathcal{V}$ could provide a more definitive indication of its nature. If no stars were to be detected, it cannot be a UCD, since such objects are gravitationally dominated by their stars. However, this is beyond the reach of current optical and near-IR observing facilities.

Cylindrical mass profile

Supplementary Figure 1 displays the cylindrical mass profiles for most tested models.

Posterior distributions

Supplementary Figures 2 to 24 display the posterior distribution for the parameters of all the mass density profiles tested for detection $\mathcal{V}$. Note that in most of these plots, we use the projected mass within 90 pc as the amplitude parameter because it is very well constrained and almost independent of the other parameters.

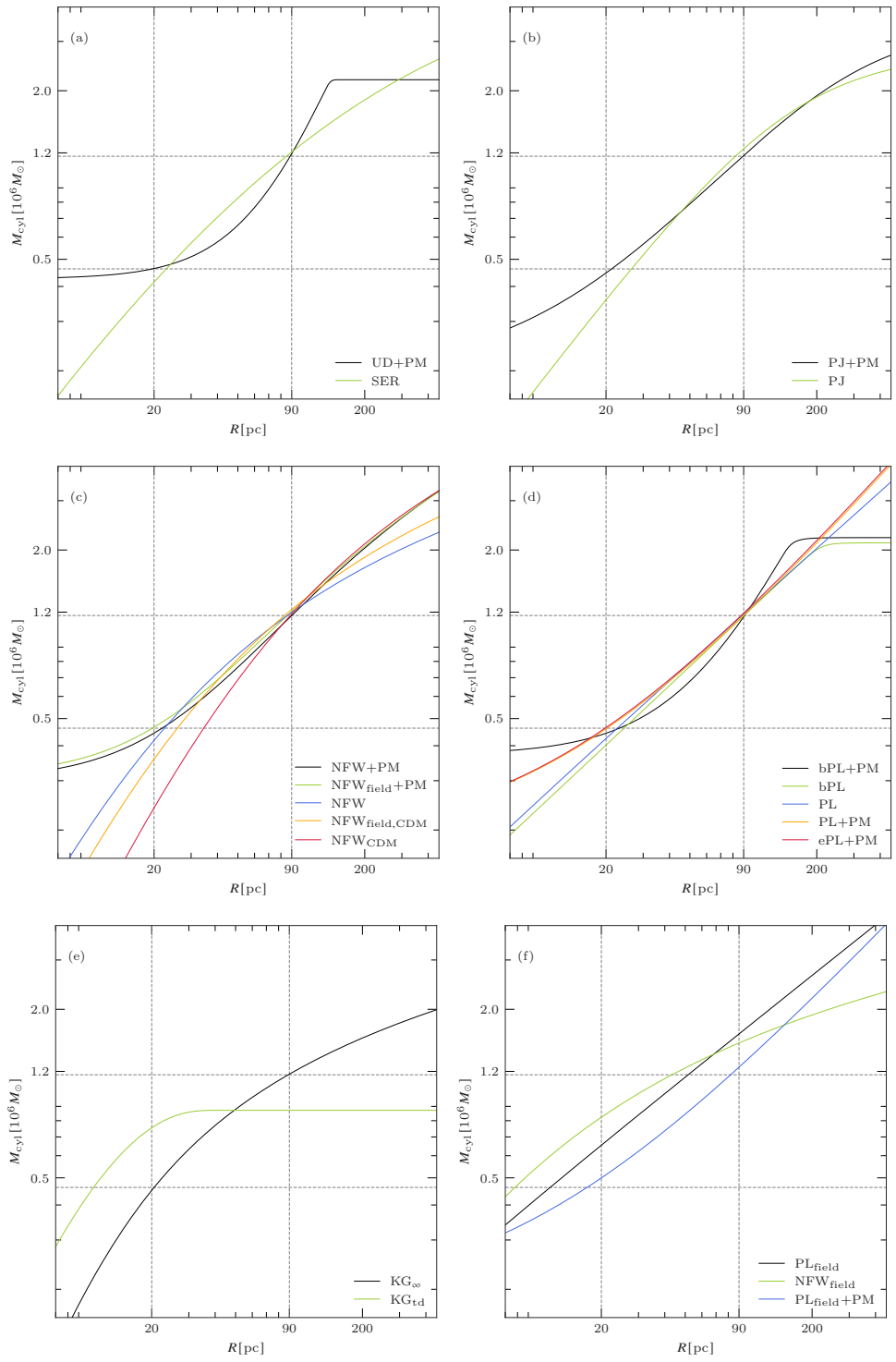

Supplementary Figure 1 Cylindrical mass profiles. Panel (a): cylindrical mass profiles for the uniform disk plus point mass and Sérsic models. Panel (b): cylindrical mass profiles for the Pseudo-Jaffe models. Panel (c): cylindrical mass profiles for the NFW models with a redshift consistent with that of the main lens. Panel (d): cylindrical mass profiles for the power-law models. Panel (e): cylindrical mass profiles for King models. We do not plot the KG model because it is indistinguishable from the KG$_\infty$ one at this plotting scale. Panel (f): cylindrical mass profiles for the profiles with the redshift as a free parameter. In all panels, the vertical lines represent the 20 and 90 pc radii, which are also where the different models agree most closely. The horizontal lines are the corresponding values of $M_{\rm cyl}$ for the UD+PM model. In the legends, models appear in order of decreasing Bayes factor. The uncertainty bands represent the 1-σ confidence interval around the mean.

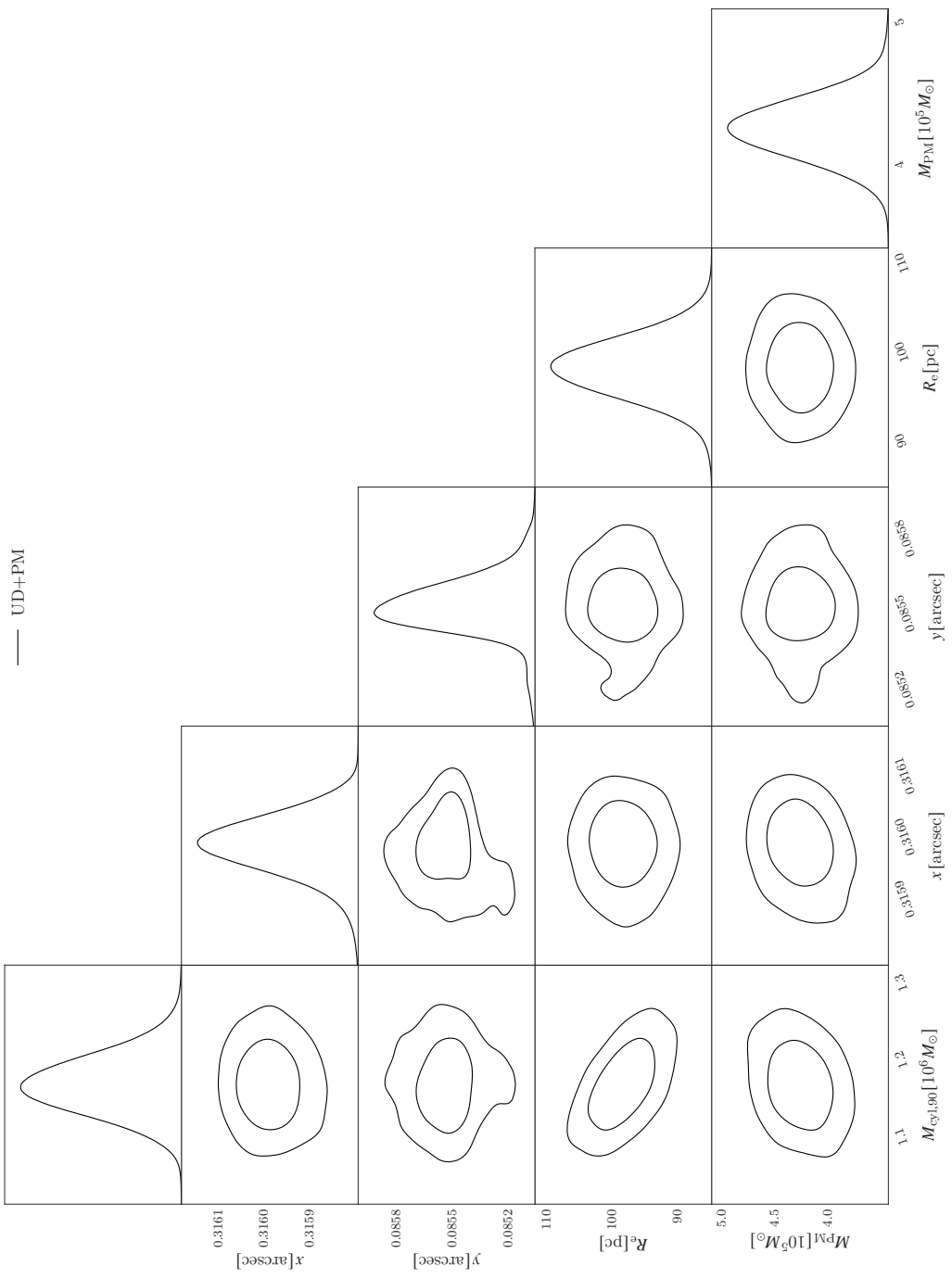

Supplementary Figure 2 Posterior distributions for the parameters of the uniform disk plus point-mass model. The contours represent the 1- and 2-σ confidence regions.

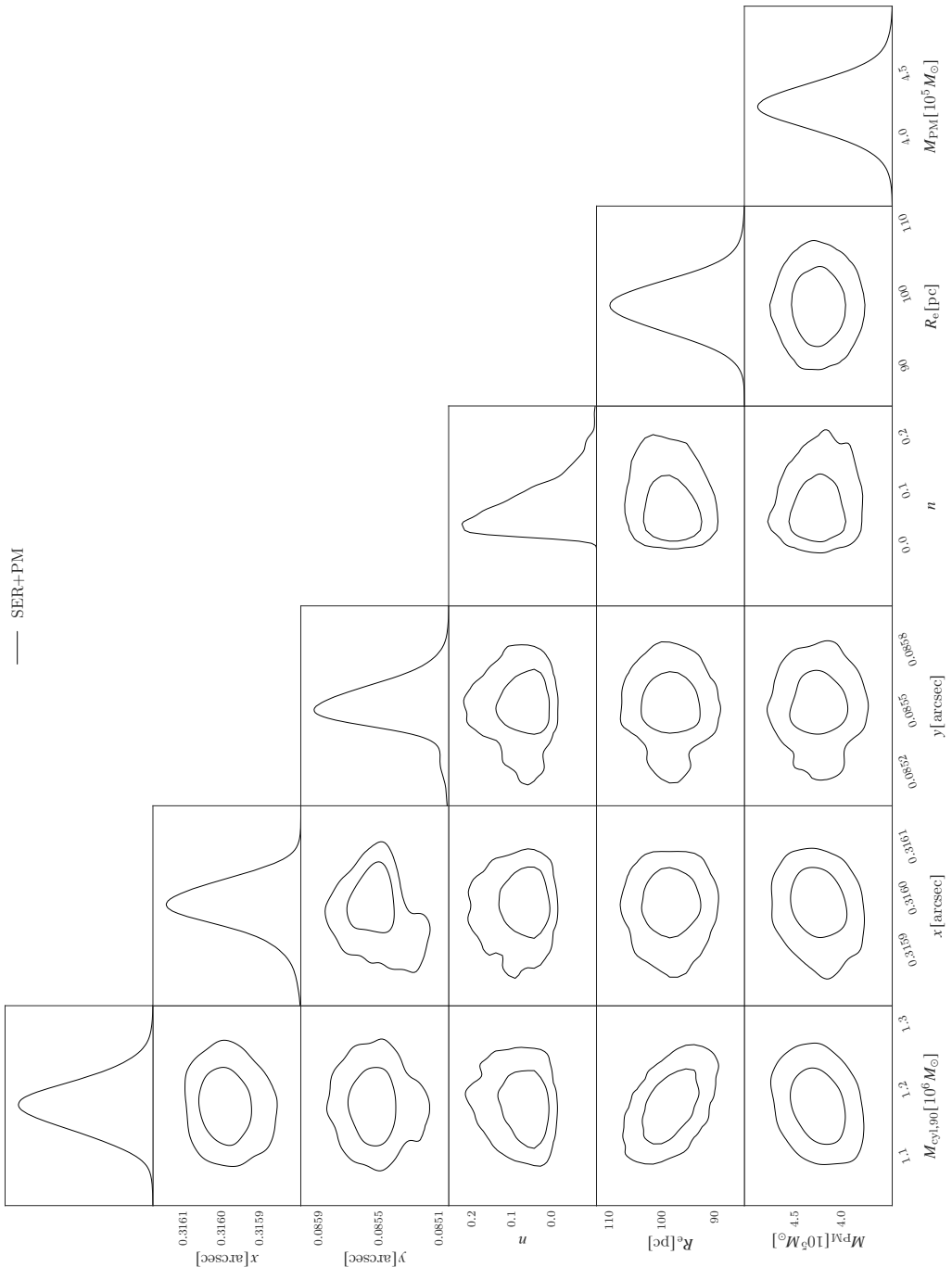

Supplementary Figure 3 Posterior distributions for the parameters of the Sérsic plus point-mass model. The contours represent the 1- and 2-σ confidence regions.

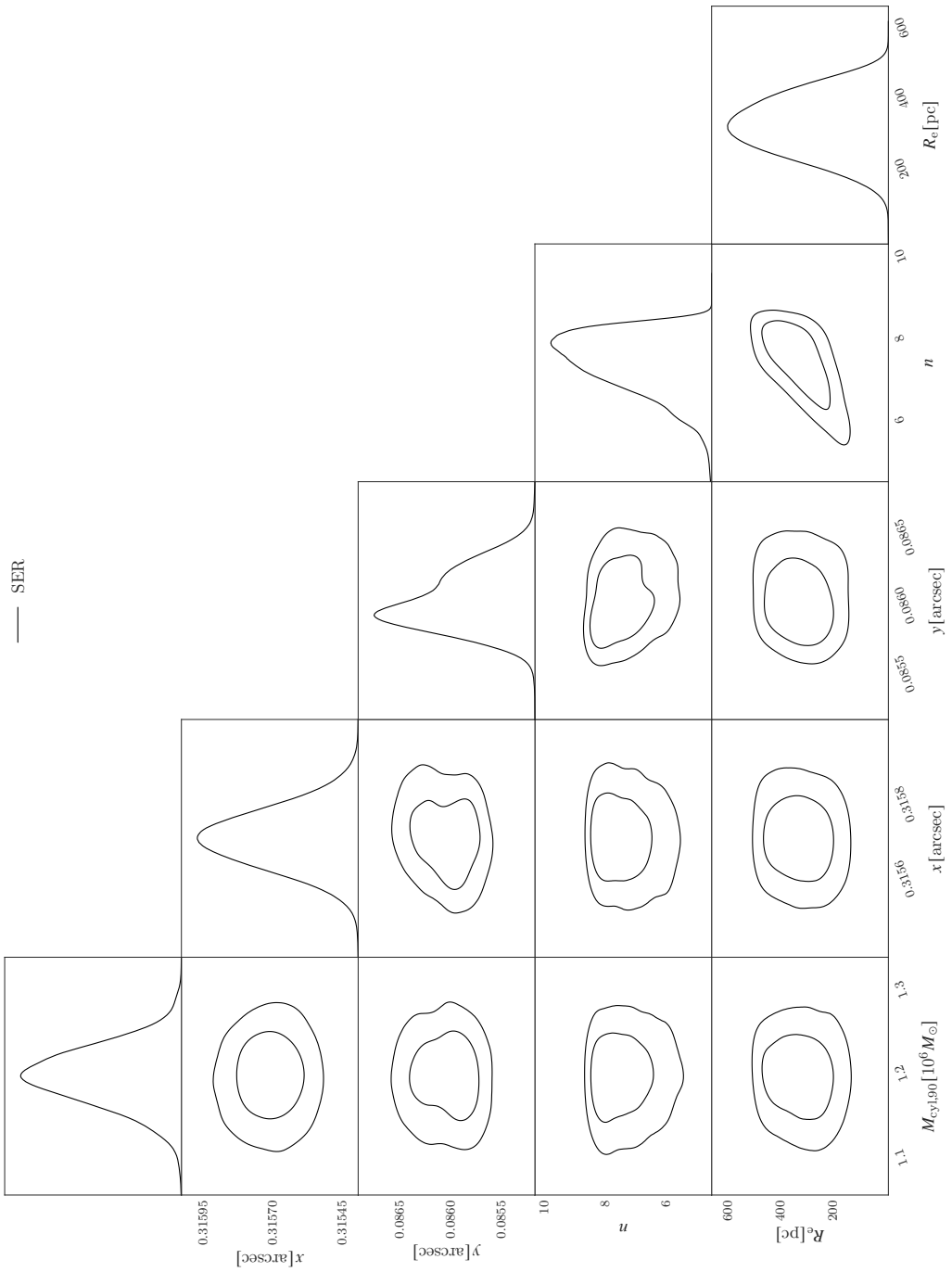

Supplementary Figure 4 Posterior distributions for the parameters of the Sérsic model. The contours represent the 1- and 2-σ confidence regions.

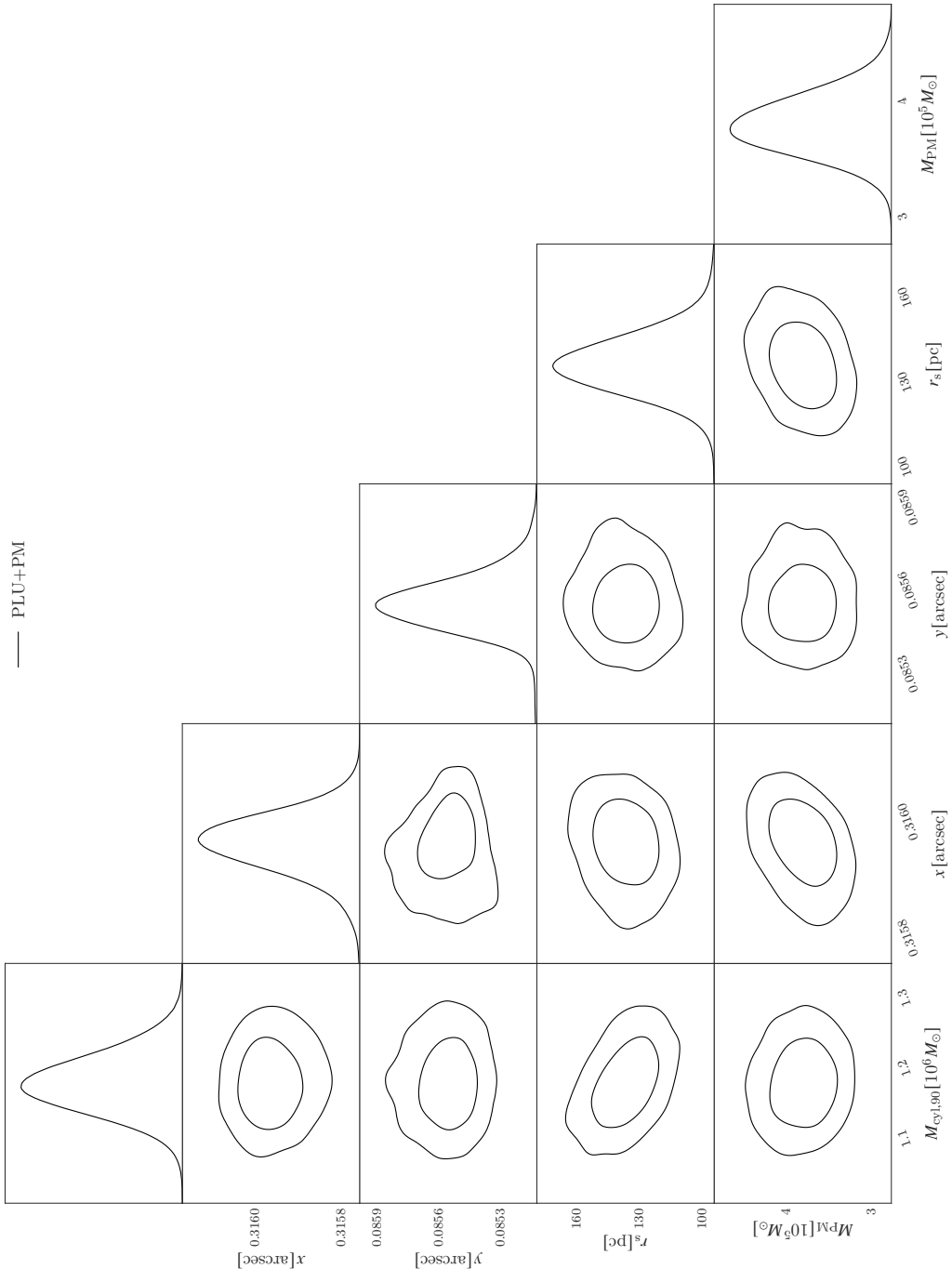

Supplementary Figure 5 Posterior distributions for the parameters of the Plummer plus point-mass model. The contours represent the 1- and 2-σ confidence regions.

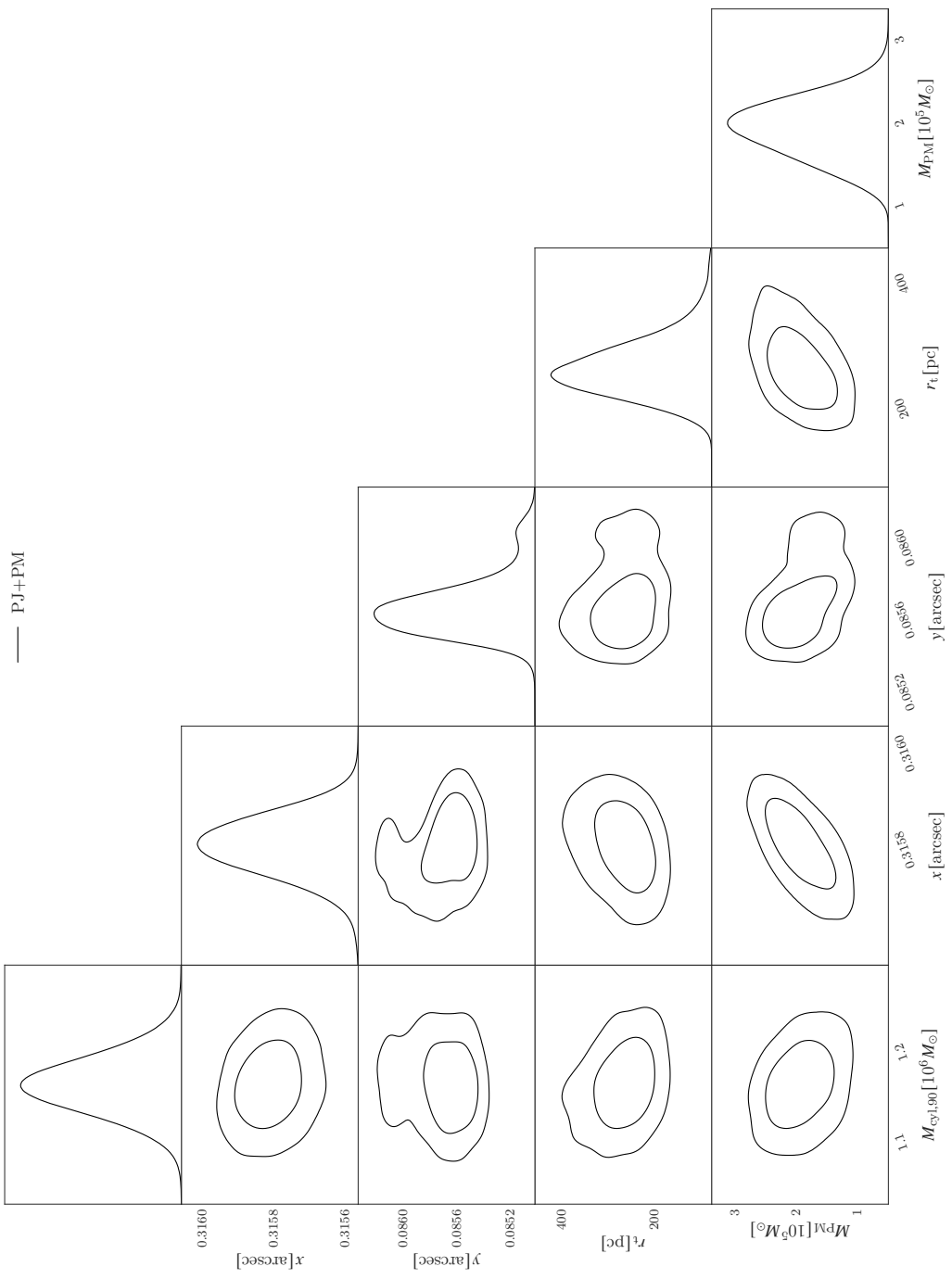

Supplementary Figure 6 Posterior distributions for the parameters of the Pseudo-Jaffe plus point-mass model. The contours represent the 1- and 2-σ confidence regions.

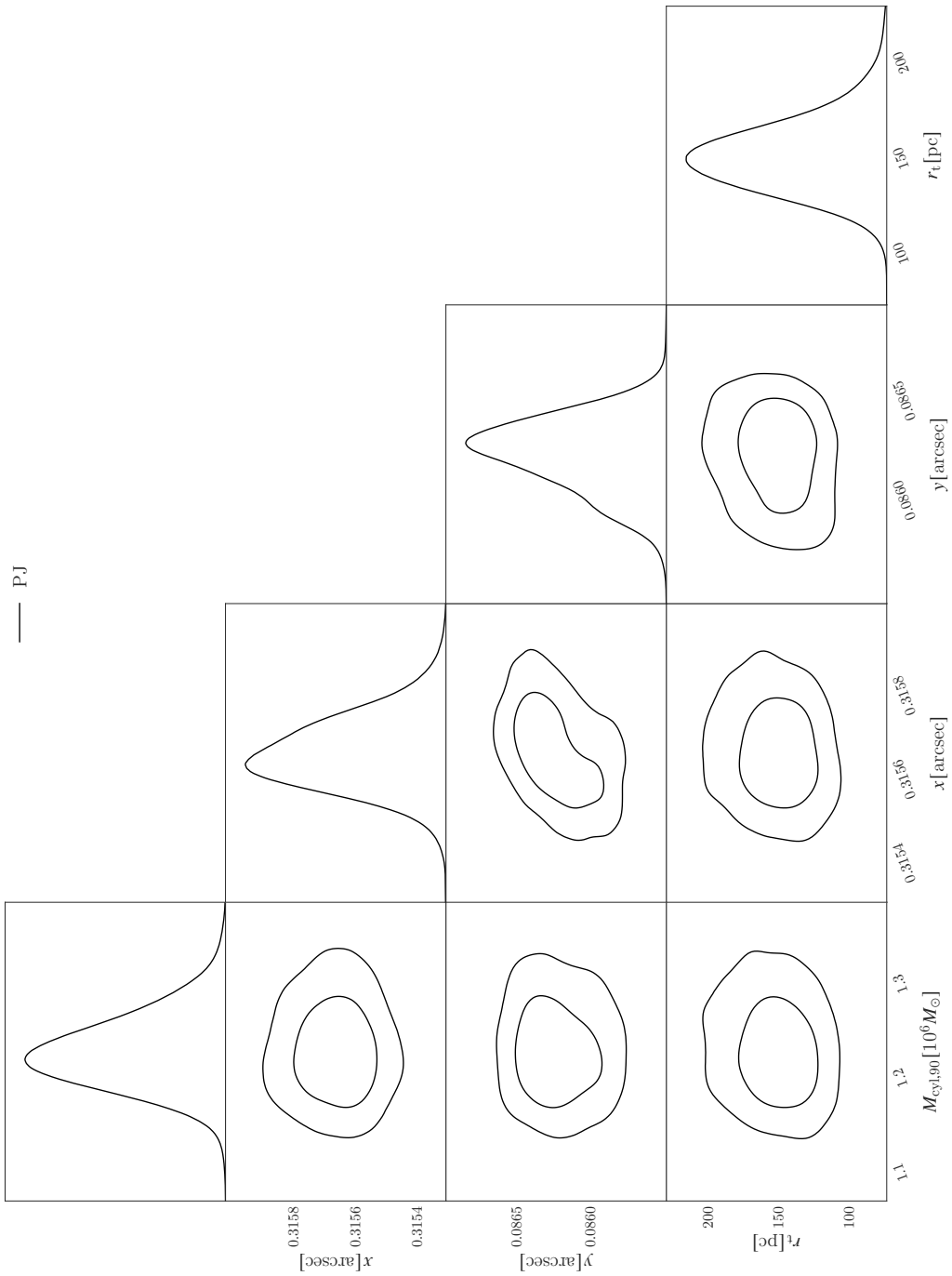

Supplementary Figure 7 Posterior distributions for the parameters of the Pseudo-Jaffe model. The contours represent the 1- and 2-σ confidence regions.

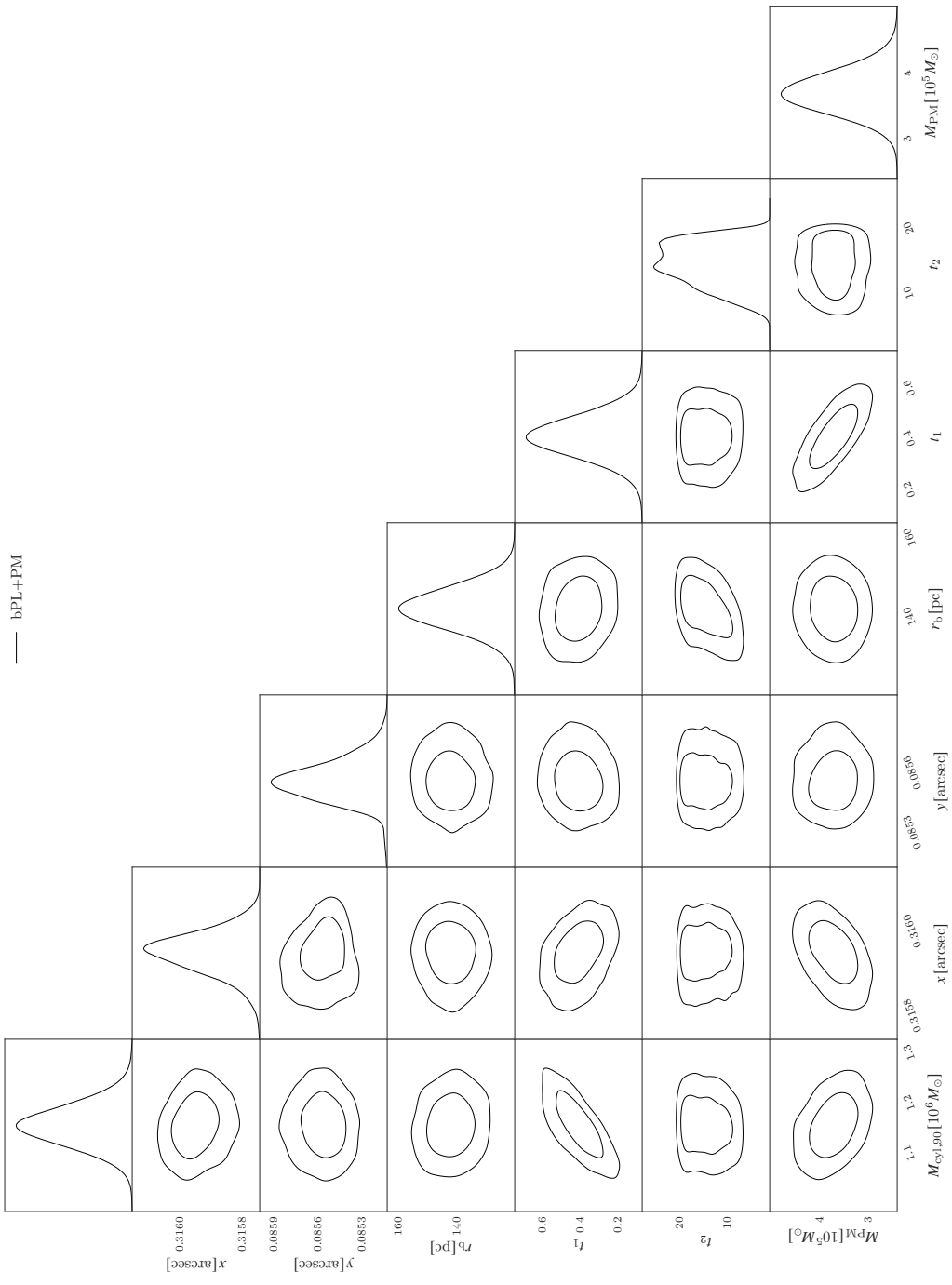

Supplementary Figure 8 Posterior distributions for the parameters of the broken power-law plus point-mass model. The contours represent the 1- and 2-σ confidence regions.

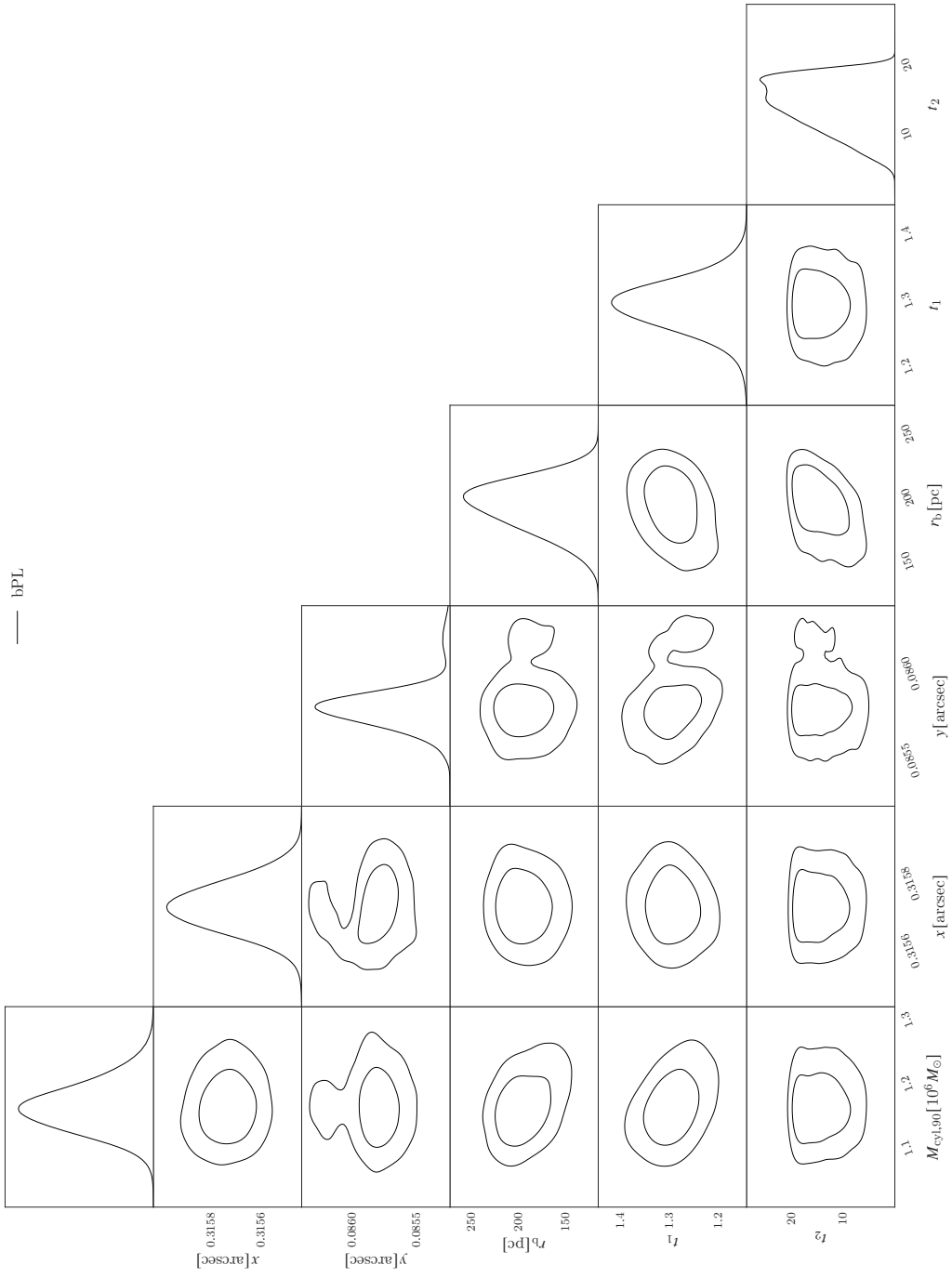

Supplementary Figure 9 Posterior distributions for the parameters of the broken power-law model. The contours represent the 1- and 2-σ confidence regions.

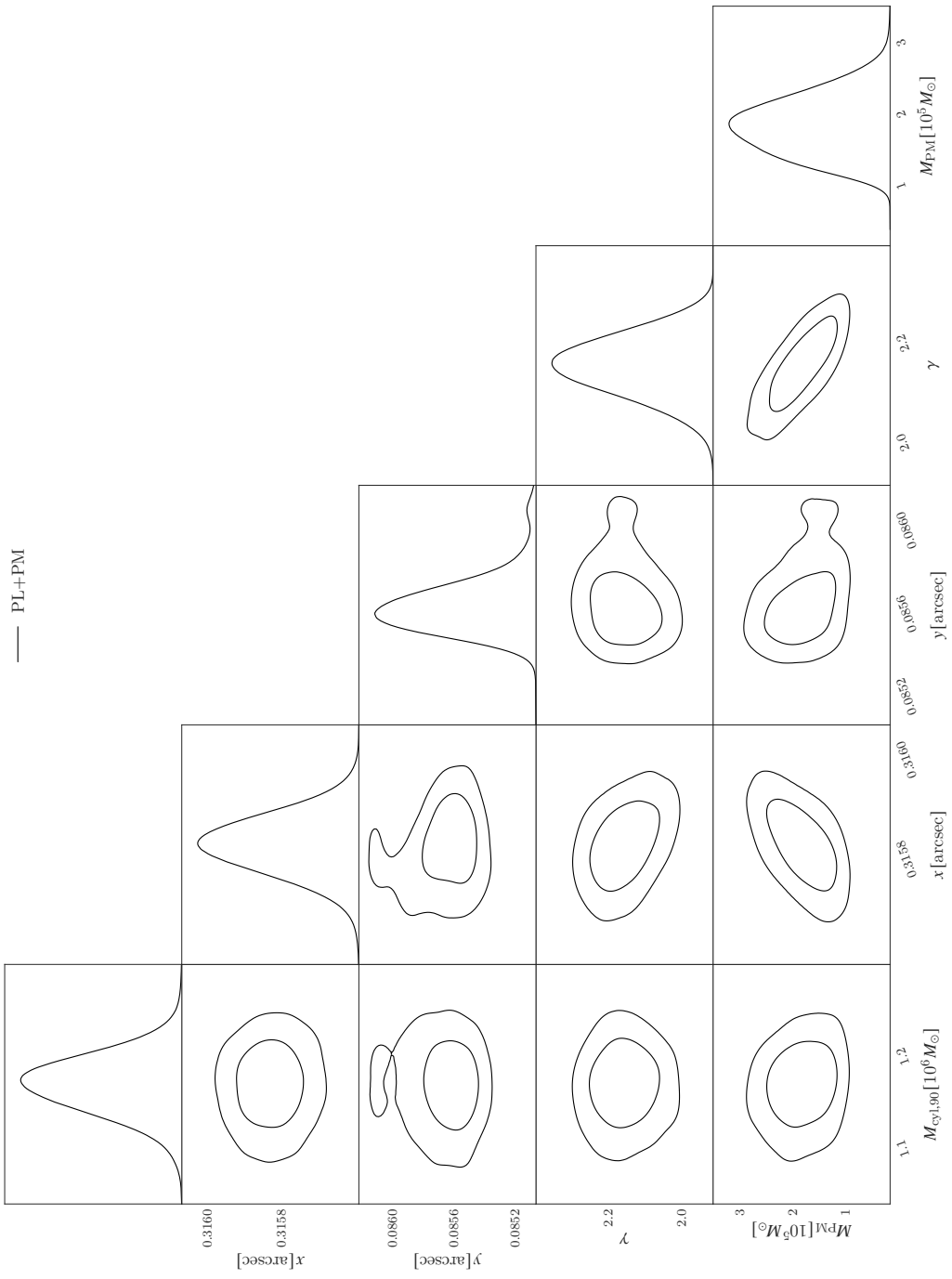

Supplementary Figure 10 Posterior distributions for the parameters of the power-law plus point-mass model. The contours represent the 1- and 2-σ confidence regions.

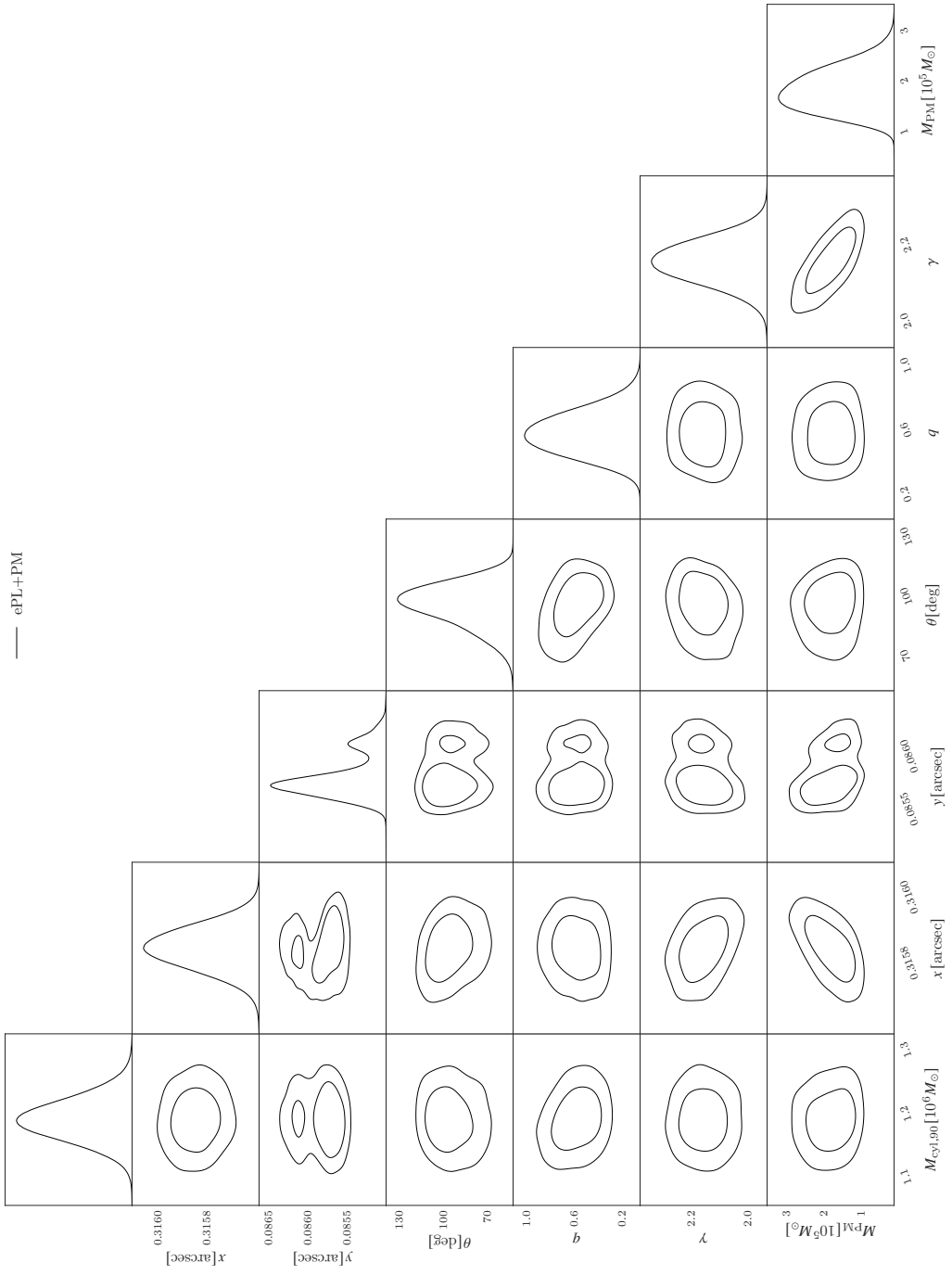

Supplementary Figure 11 Posterior distributions for the parameters of the elliptical power-law plus point-mass model. The contours represent the 1- and 2-σ confidence regions.

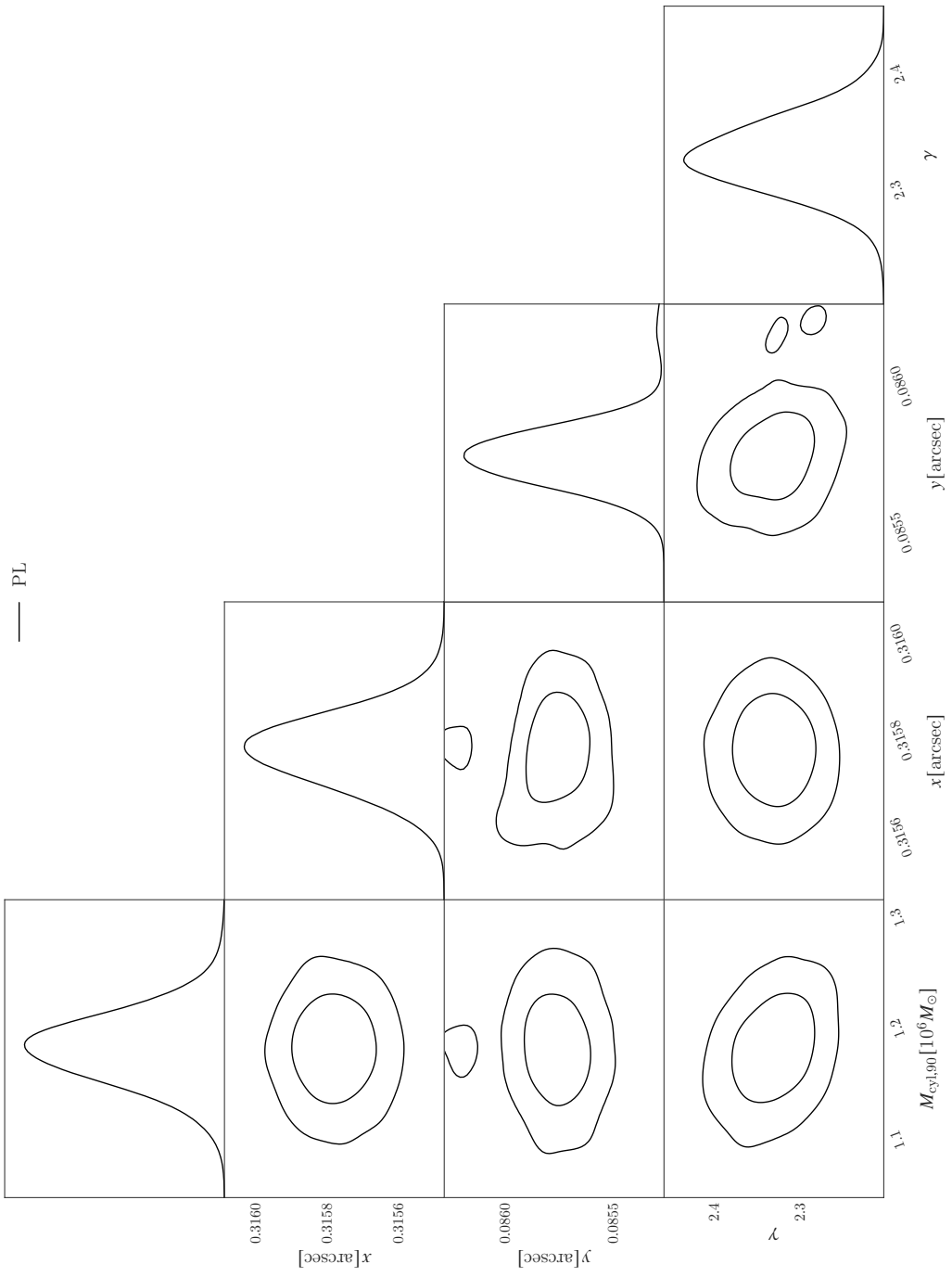

Supplementary Figure 12 Posterior distributions for the parameters of the power-law model. The contours represent the 1- and 2-σ confidence regions.

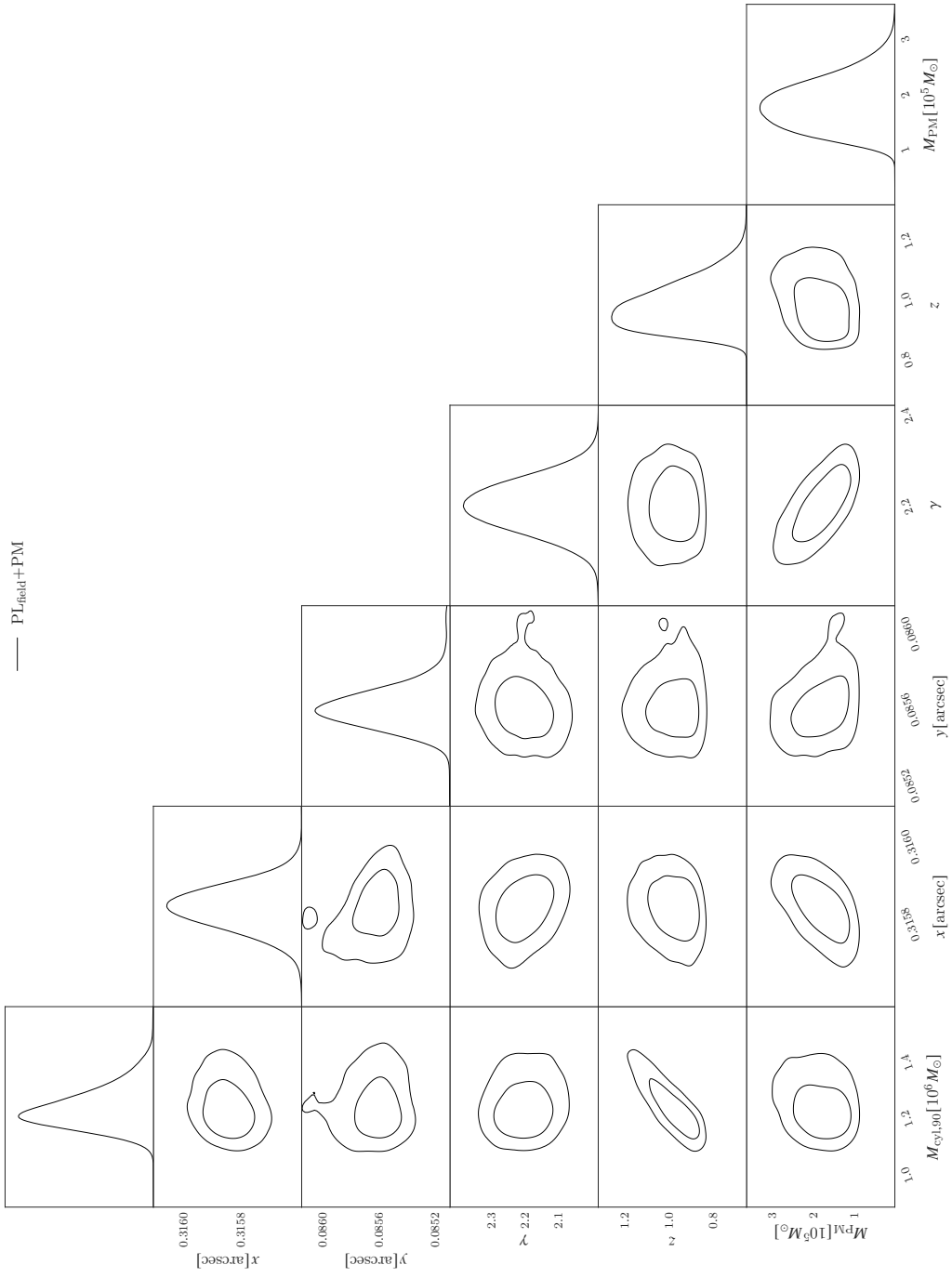

Supplementary Figure 13 Posterior distributions for the parameters of the free-redshift power-law plus point mass model. The contours represent the 1- and 2-σ confidence regions.

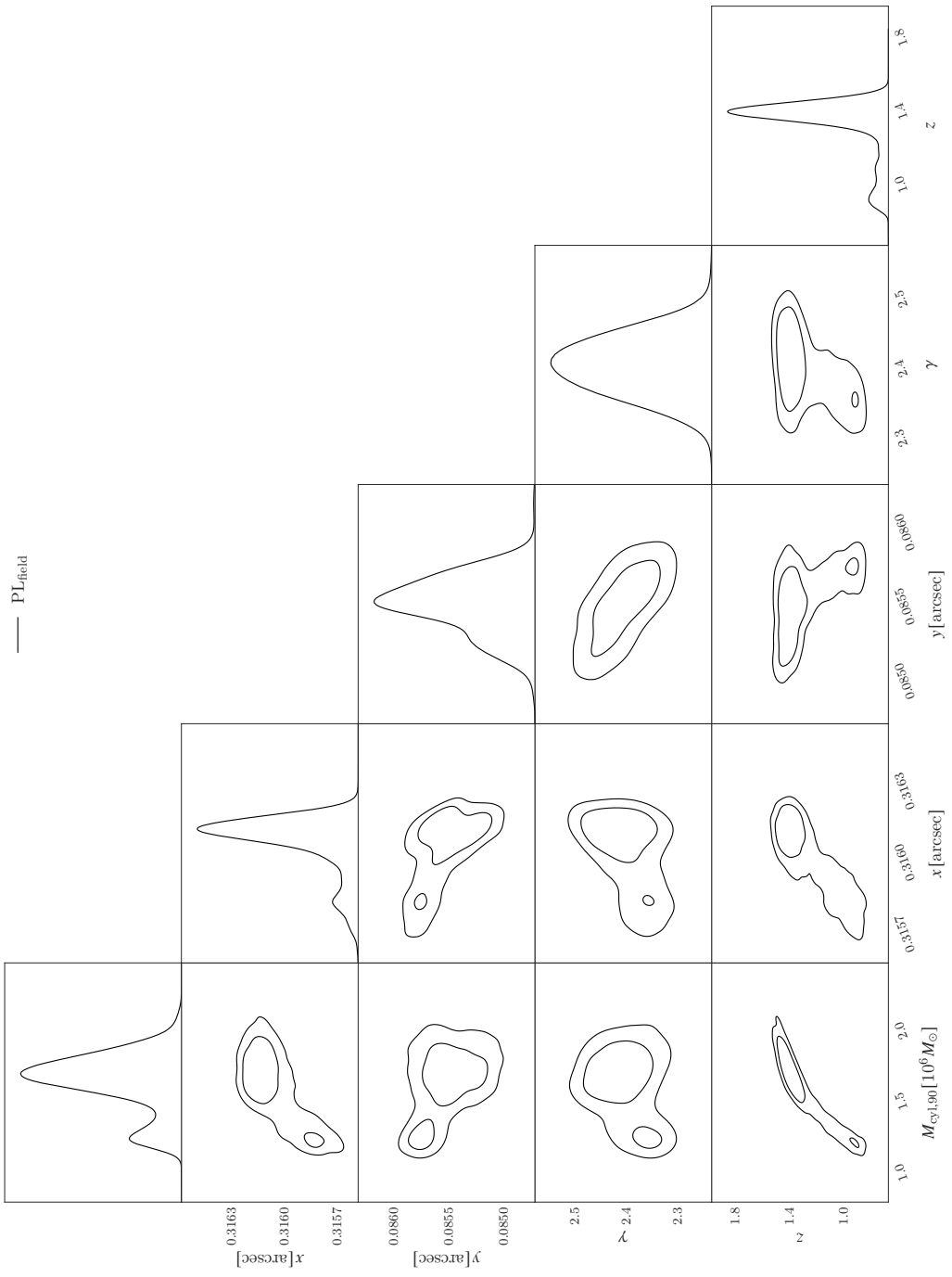

Supplementary Figure 14 Posterior distributions for the parameters of the free-redshift power-law model. The contours represent the 1- and 2-σ confidence regions.

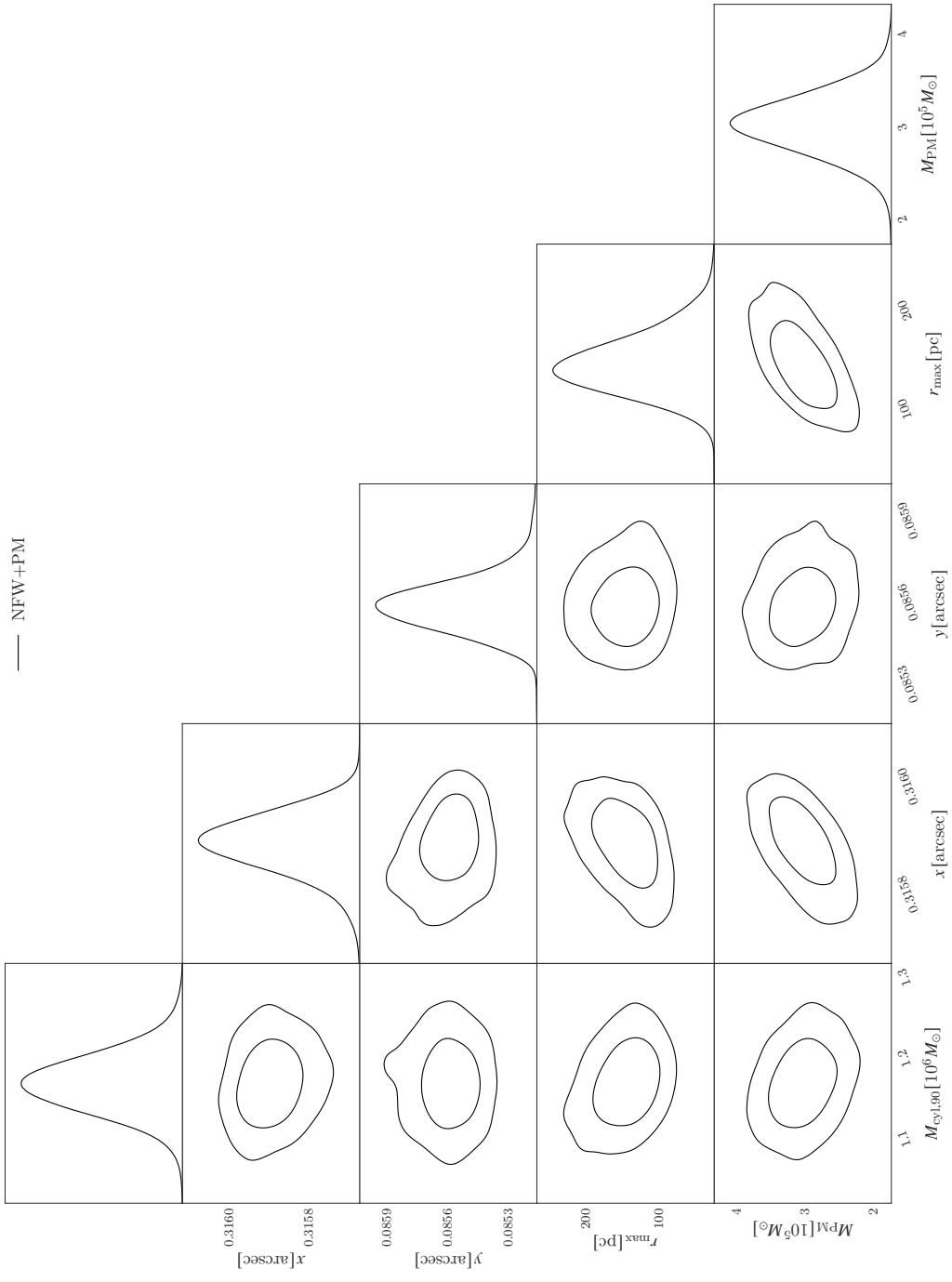

Supplementary Figure 15 Posterior distributions for the parameters of the NFW plus point mass model. The contours represent the 1- and 2-σ confidence regions.

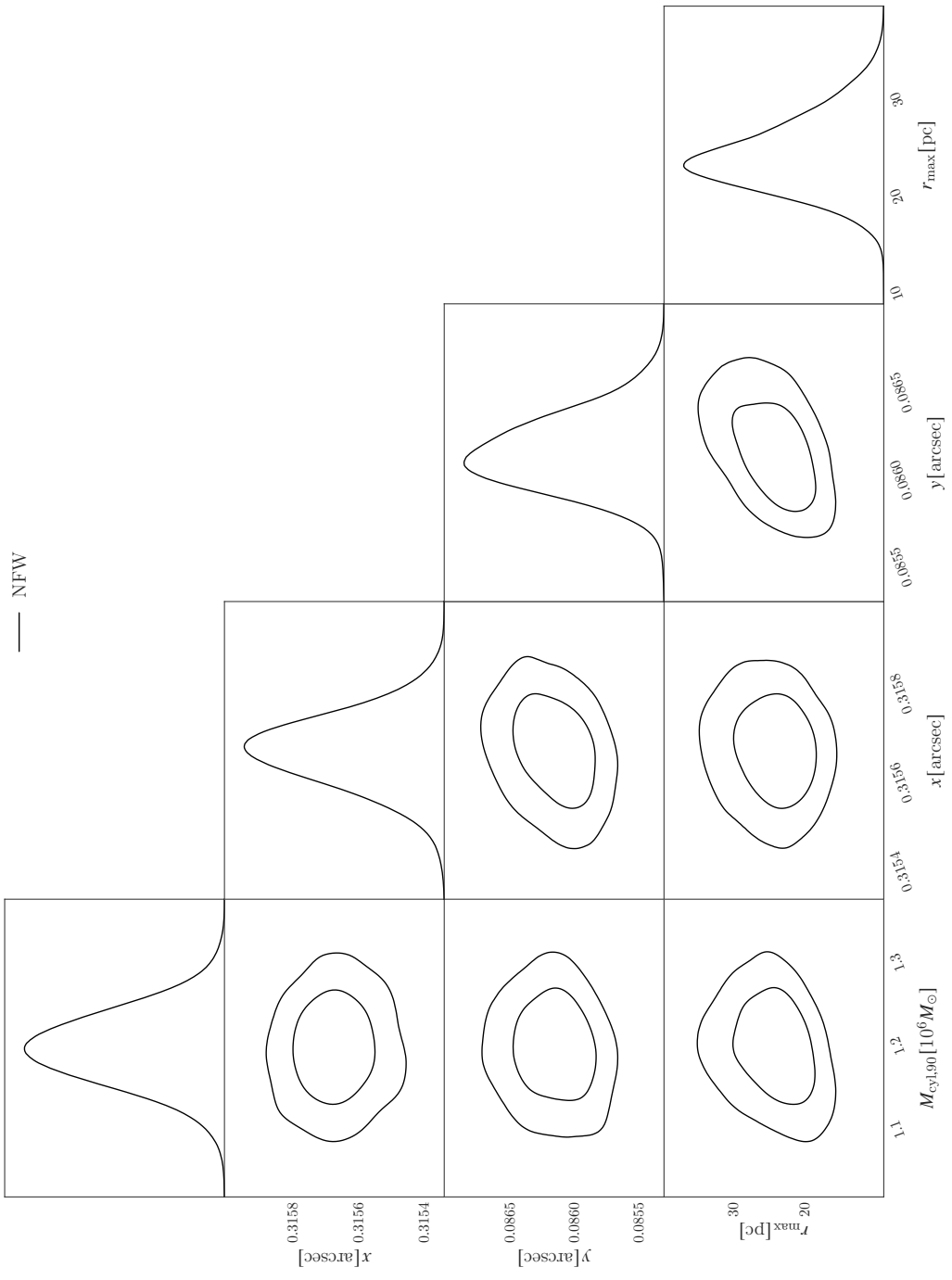

Supplementary Figure 16 Posterior distributions for the parameters of the NFW model. The contours represent the 1- and 2-σ confidence regions.

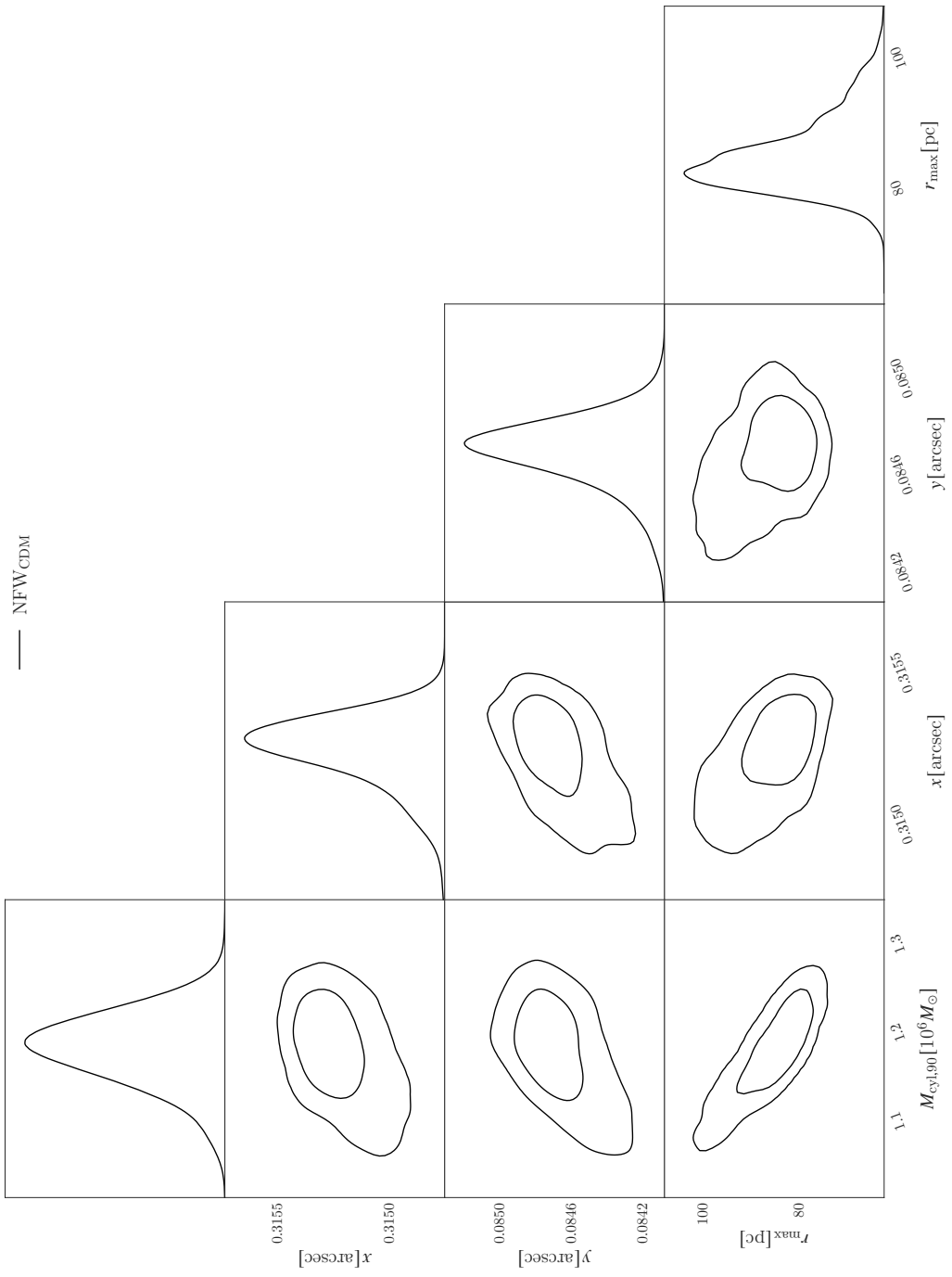

Supplementary Figure 17 Posterior distributions for the parameters of the NFW$_{\rm CDM}$ model. The contours represent the 1- and 2-σ confidence regions. The prior on the $r_{\rm max}$ is informed by CDM simulations.

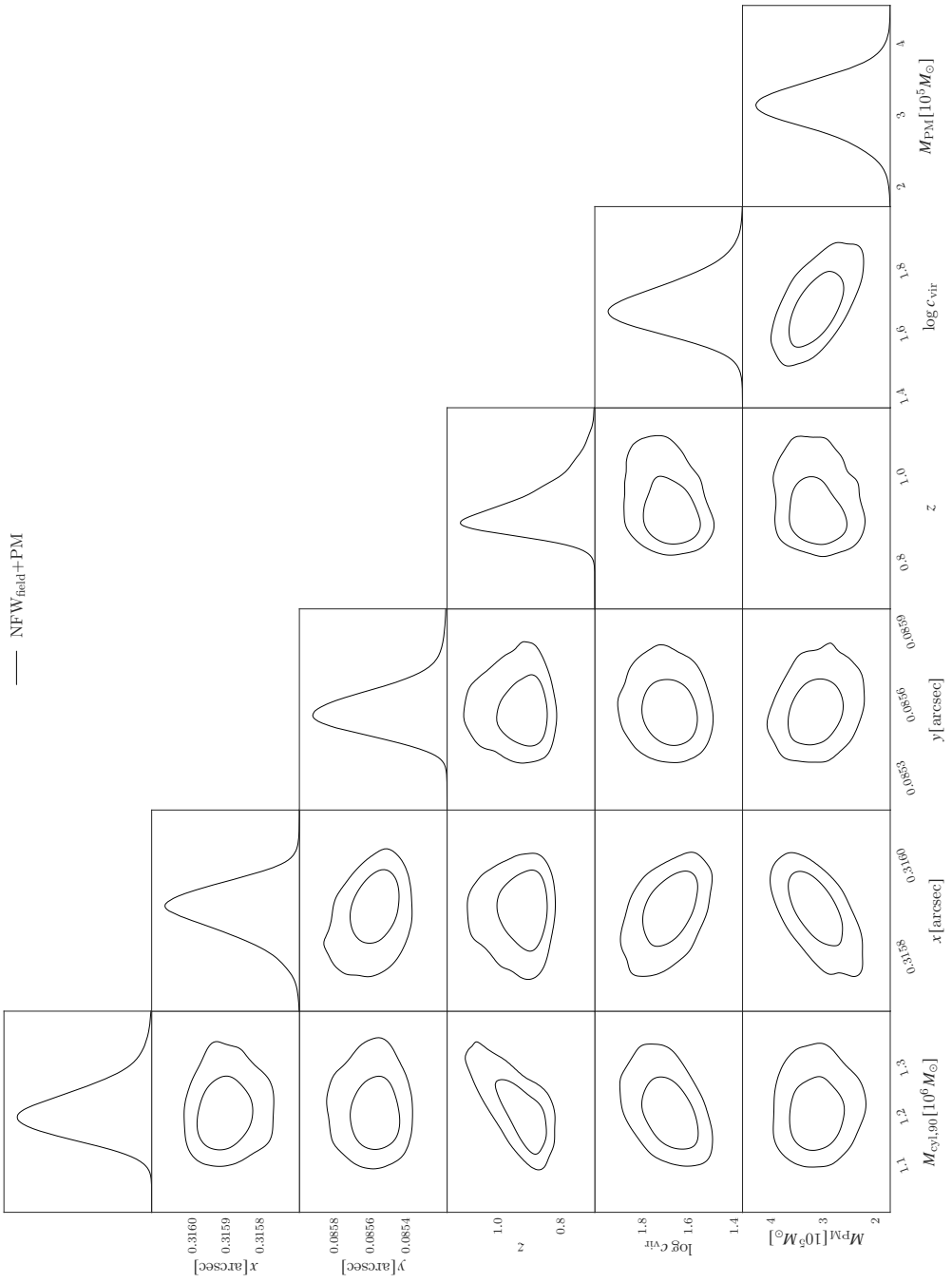

Supplementary Figure 18 Posterior distributions for the parameters of the free-redshift NFW plus point mass model. The contours represent the 1- and 2-σ confidence regions.

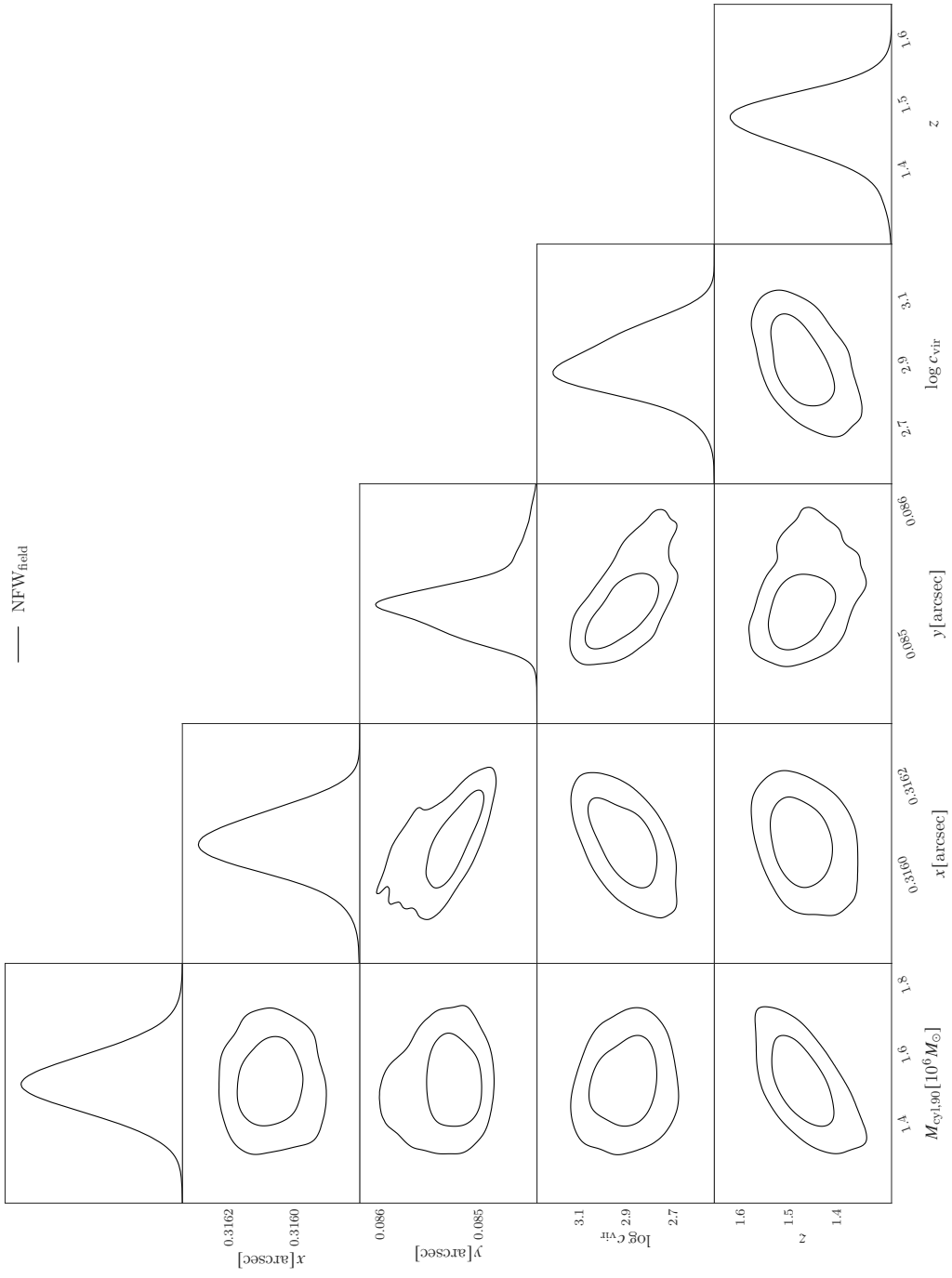

Supplementary Figure 19 Posterior distributions for the parameters of the free-redshift NFW model. The contours represent the 1- and 2-σ confidence regions.

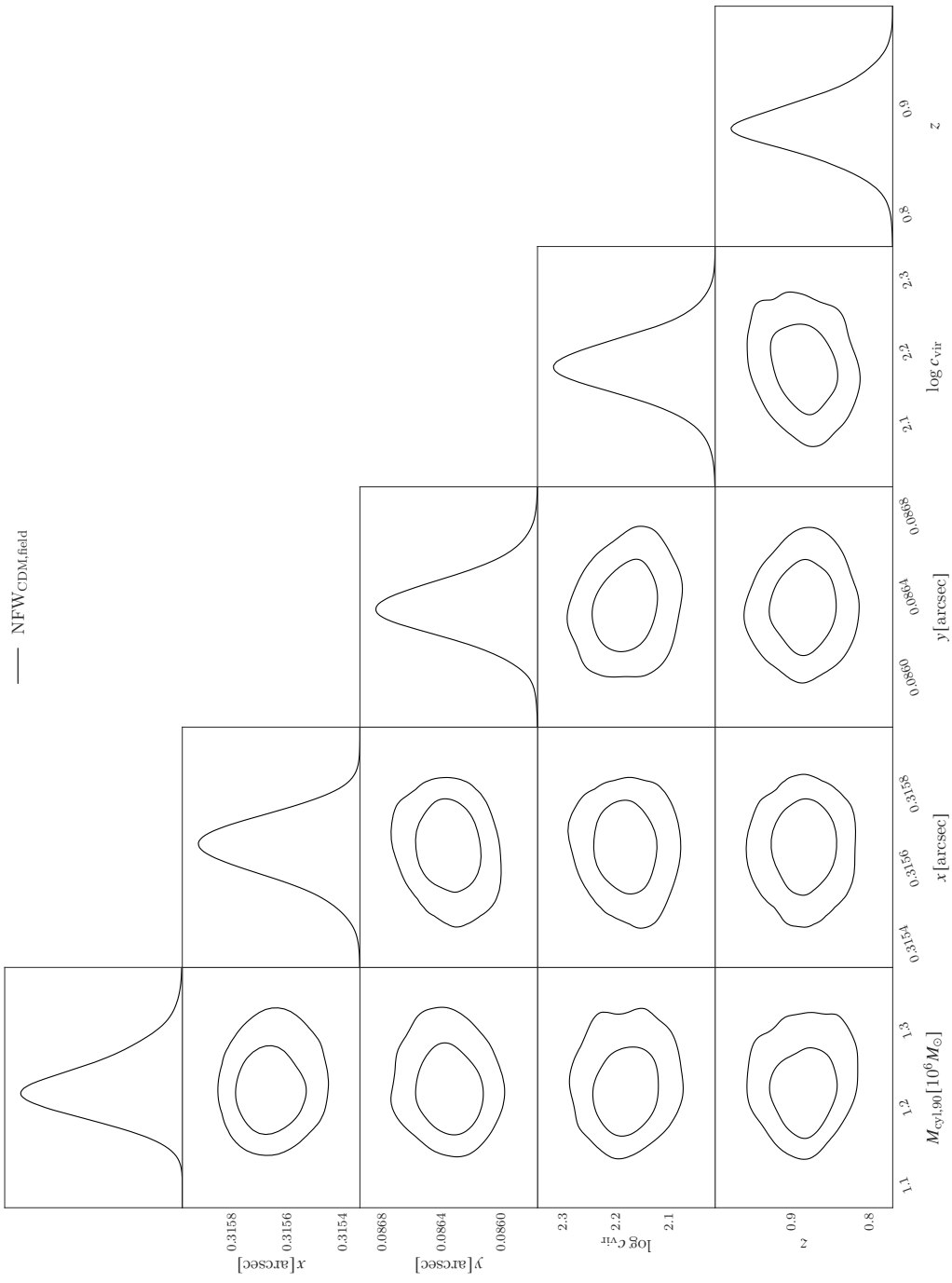

Supplementary Figure 20 Posterior distributions for the parameters of the free-redshift NFW$_{\rm CDM}$ model. The contours represent the 1- and 2-σ confidence regions.

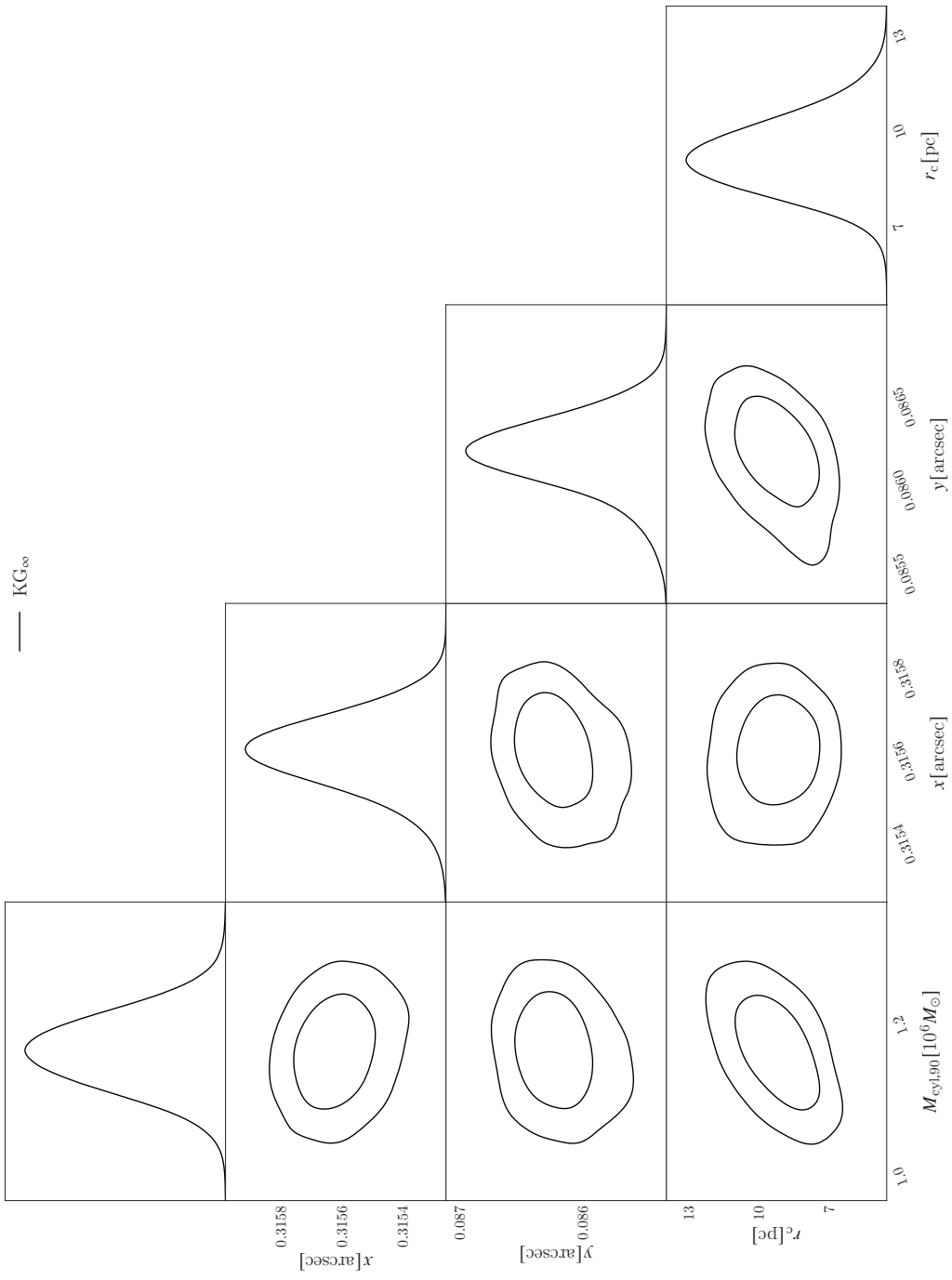

Supplementary Figure 21 Posterior distributions for the parameters of the KG$_\infty$ model. The contours represent the 1- and 2-σ confidence regions. The truncation radius is assumed to $r_{\rm t} \to \infty$.

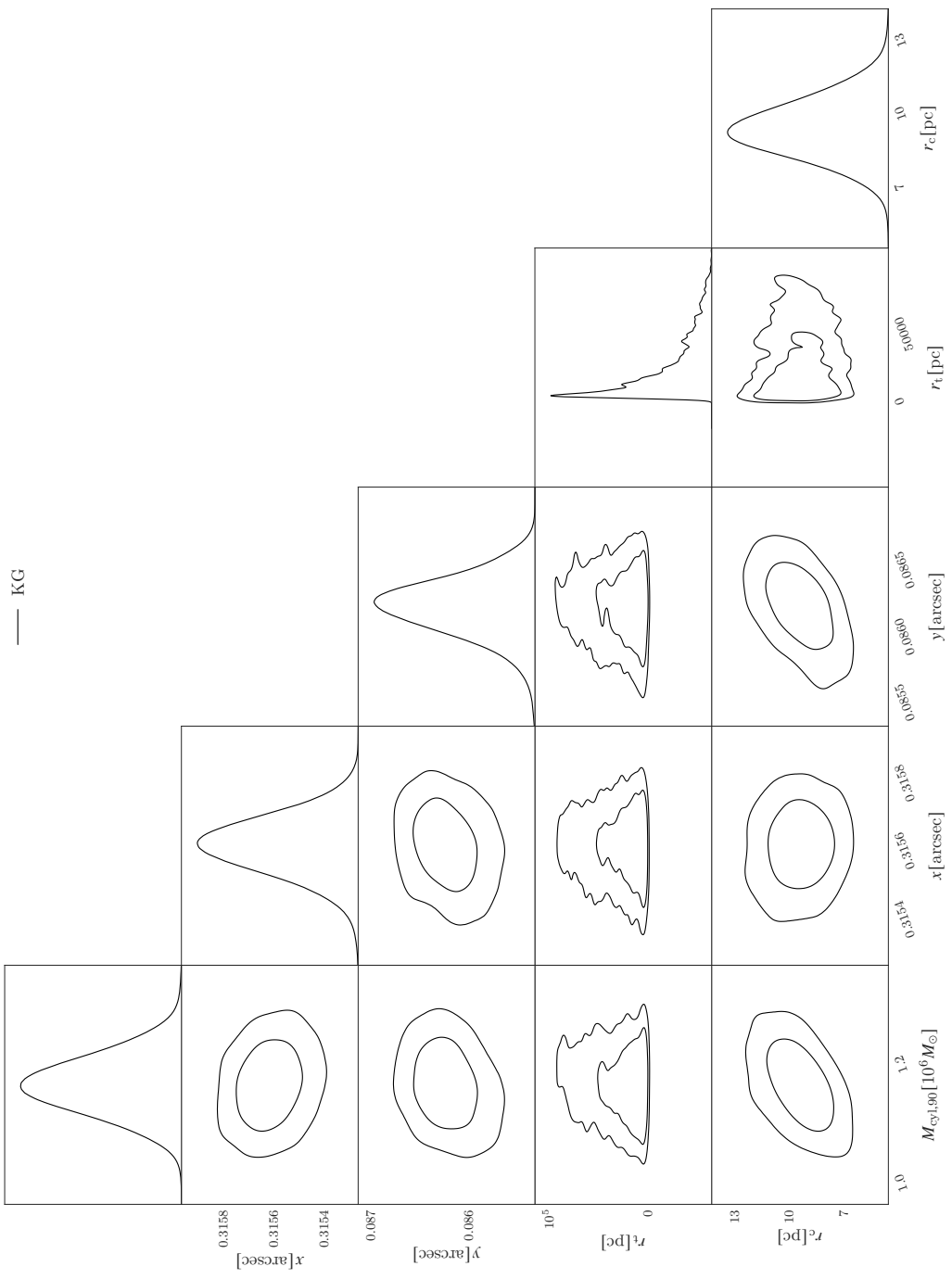

Supplementary Figure 22 Posterior distributions for the parameters of the KG model. The contours represent the 1- and 2-σ confidence regions.

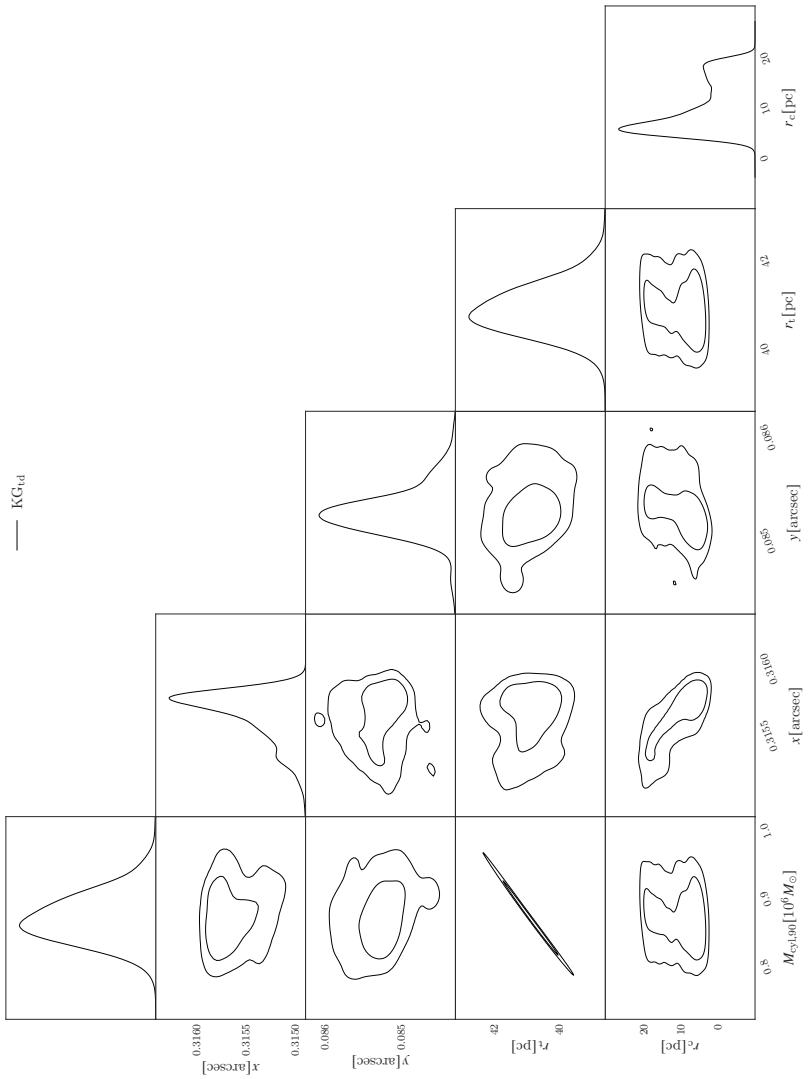

Supplementary Figure 23 Posterior distributions for the parameters of the KG$_{\rm td}$ model. The contours represent the 1- and 2-σ confidence regions. The truncation radius is assumed to be the same as the tidal radius.

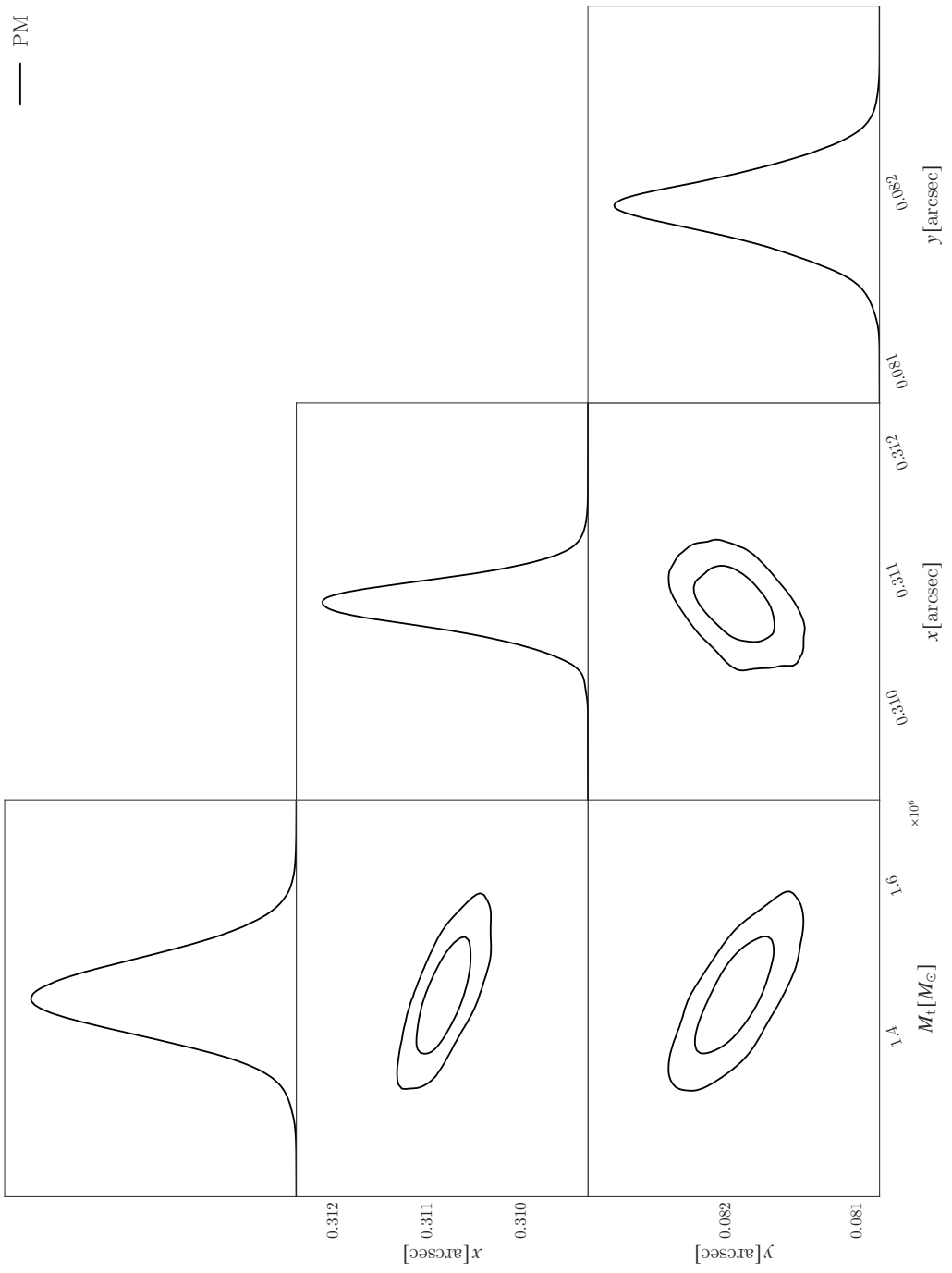

Supplementary Figure 24 Posterior distributions for the parameters of the point mass model. The contours represent the 1- and 2-σ confidence regions.

References

[1] Powell, D., et al.: A million-solar-mass object detected at a cosmological distance using gravitational imaging. Nat. Astron. (2025)

[2] Duffy, A.R., Schaye, J., Kay, S.T., Dalla Vecchia, C.: Dark matter halo concentrations in the Wilkinson Microwave Anisotropy Probe year 5 cosmology. Mon. Not. R. Astron. Soc. **390**(1), 64–68 (2008)

[3] Ludlow, A.D., et al.: The mass-concentration-redshift relation of cold and warm dark matter haloes. Mon. Not. R. Astron. Soc. **460**(2), 1214–1232 (2016)

[4] Moliné, Á., et al.: ΛCDM halo substructure properties revealed with high-resolution and large-volume cosmological simulations. Mon. Not. R. Astron. Soc. **518**(1), 157–173 (2023)

[5] Outmezguine, N.J., Boddy, K.K., Gad-Nasr, S., Kaplinghat, M., Sagunski, L.: Universal gravothermal evolution of isolated self-interacting dark matter halos for velocity-dependent cross-sections. Mon. Not. R. Astron. Soc. **523**(3), 4786–4800 (2023)

[6] Yang, D., Nadler, E.O., Yu, H.-B., Zhong, Y.-M.: A parametric model for self-interacting dark matter halos. J. Cosmol. Astropart. Phys. **2024**(2), 032 (2024)

[7] Ando, S., Horigome, S., Nadler, E.O., Yang, D., Yu, H.-B.: A parametric model for self-interacting dark matter halos. J. Cosmol. Astropart. Phys. **2025**(2), 053 (2025)

[8] Turner, H.C., Lovell, M.R., Zavala, J., Vogelsberger, M.: The onset of gravothermal core collapse in velocity-dependent self-interacting dark matter subhaloes. Mon. Not. R. Astron. Soc. **505**(4), 5327–5339 (2021)

[9] Gad-Nasr, S., Boddy, K.K., Kaplinghat, M., Outmezguine, N.J., Sagunski, L.: On the late-time evolution of velocity-dependent self-interacting dark matter halos. J. Cosmol. Astropart. Phys. **2024**(5), 131 (2024)

[10] He, Q., et al.: Globular clusters versus dark matter haloes in strong lensing observations. Mon. Not. R. Astron. Soc. **480**(4), 5084–5091 (2018)

[11] Lagattuta, D.J., et al.: SHARP - I. A high-resolution multiband view of the infrared Einstein ring of JVAS B1938+666. Mon. Not. R. Astron. Soc. **424**(4), 2800–2810 (2012)

[12] Saifollahi, T., et al.: Euclid: Early Release Observations – Globular clusters in the Fornax galaxy cluster, from dwarf galaxies to the intracluster field. Astron. Astrophys. **697**, 10 (2025)

[13] Jordán, A., et al.: The ACS Virgo Cluster Survey XVI. Selection Procedure and

Catalogs of Globular Cluster Candidates. Astrophys. J. Suppl. Ser. **180**(1), 54–66 (2009)

[14] Hsueh, J.-W., et al.: SHARP - VII. New constraints on the dark matter free-streaming properties and substructure abundance from gravitationally lensed quasars. Mon. Not. R. Astron. Soc. **492**(2), 3047–3059 (2020)

[15] Despali, G., Vegetti, S., White, S.D.M., Giocoli, C., van den Bosch, F.C.: Modelling the line-of-sight contribution in substructure lensing. Mon. Not. R. Astron. Soc. **475**(4), 5424–5442 (2018)

[16] Ripepi, V., et al.: On the Remote Galactic Globular Cluster NGC 2419. Astrophys. J. Lett. **667**(1), 61–64 (2007)

[17] Harris, W.E.: A New Catalog of Globular Clusters in the Milky Way (2010).

[18] Meylan, G., Heggie, D.C.: Internal dynamics of globular clusters. Astron. Astrophys. Rev. **8**, 1–143 (1997)

[19] Massari, D., et al.: Euclid: Early Release Observations – Unveiling the morphology of two Milky Way globular clusters out to their periphery. Astron. Astrophys. **697**, A8 (2025)

[20] Hilker, M., Infante, L., Vieira, G., Kissler-Patig, M., Richtler, T.: The central region of the Fornax cluster. II. Spectroscopy and radial velocities of member and background galaxies. Astron. Astrophys. Suppl. **134**, 75–86 (1999)

[21] Phillipps, S., Drinkwater, M.J., Gregg, M.D., Jones, J.B.: Ultracompact Dwarf Galaxies in the Fornax Cluster. Astrophys. J. **560**(1), 201–206 (2001)

[22] Drinkwater, M.J., et al.: A class of compact dwarf galaxies from disruptive processes in galaxy clusters. Nature **423**(6939), 519–521 (2003)

[23] Haşegan, M., et al.: The ACS Virgo Cluster Survey. VII. Resolving the Connection between Globular Clusters and Ultracompact Dwarf Galaxies. Astrophys. J. **627**(1), 203–223 (2005)

[24] Mieske, S., et al.: The nature of UCDs: Internal dynamics from an expanded sample and homogeneous database. Astron. Astrophys. **487**(3), 921–935 (2008)

[25] Misgeld, I., Hilker, M.: Families of dynamically hot stellar systems over 10 orders of magnitude in mass. Mon. Not. R. Astron. Soc. **414**(4), 3699–3710 (2011)

[26] Norris, M.A., et al.: The AIMSS Project - I. Bridging the star cluster-galaxy divide. Mon. Not. R. Astron. Soc. **443**(2), 1151–1172 (2014)

[27] Norris, M.A., Kannappan, S.J.: The ubiquity and dual nature of ultra-compact dwarfs. Mon. Not. R. Astron. Soc. **414**(1), 739–758 (2011)

[28] Da Rocha, C., et al.: Two formation channels of ultra-compact dwarf galaxies in Hickson compact groups. Astron. Astrophys. **525**, 86 (2011)

[29] Chilingarian, I.V., Mieske, S., Hilker, M., Infante, L.: Dynamical versus stellar masses of ultracompact dwarf galaxies in the Fornax cluster. Mon. Not. R. Astron. Soc. **412**(3), 1627–1638 (2011)

[30] Bekki, K., Couch, W.J., Drinkwater, M.J., Shioya, Y.: Galaxy threshing and the origin of ultra-compact dwarf galaxies in the Fornax cluster. Mon. Not. R. Astron. Soc. **344**(2), 399–411 (2003)

[31] Gregg, M.D., et al.: Galaxy Threshing and Ultra-Compact Dwarfs in the Fornax Cluster. Astrophys. Space Sci. **285**(1), 113–117 (2003)

[32] Goerdt, T., et al.: The formation of ultra-compact dwarf galaxies and nucleated dwarf galaxies. Mon. Not. R. Astron. Soc. **385**(4), 2136–2142 (2008)

[33] Pfeffer, J., Griffen, B.F., Baumgardt, H., Hilker, M.: Contribution of stripped nuclear clusters to globular cluster and ultracompact dwarf galaxy populations. Mon. Not. R. Astron. Soc. **444**(4), 3670–3683 (2014)

[34] Paudel, S., et al.: The creation of a massive UCD by tidal threshing from NGC 936. Mon. Not. R. Astron. Soc. **526**(1), 136–142 (2023)

[35] Wang, K., et al.: An evolutionary continuum from nucleated dwarf galaxies to star clusters. Nature **623**(7986), 296–300 (2023)

[36] Graham, A.W., et al.: Dot to dot: high-z little red dots in $M_{\rm bh}$-$M_\star$ diagrams with galaxy-morphology-specific scaling relations. Publ. Astron. Soc. Aust. **42**, e068 (2025)

[37] Hiroshima, N., Ando, S., Ishiyama, T.: Modeling evolution of dark matter substructure and annihilation boost. Physical Review D **97**(12) (2018)

[38] Ando, S., Ishiyama, T., Hiroshima, N.: Halo substructure boosts to the signatures of dark matter annihilation. Galaxies **7**(3), 68 (2019)

[39] Baumgardt, H., Hénault-Brunet, V., Dickson, N., Sollima, A.: Evidence for a bottom-light initial mass function in massive star clusters. Mon. Not. R. Astron. Soc. **521**(3), 3991–4008 (2023)

[40] Meštrić, U., et al.: Exploring the physical properties of lensed star-forming clumps at $2 \leq z \leq 6$. Monthly Notices of the Royal Astronomical Society **516**(3), 3532–3555 (2022)